VERTICAL BLOCK COPOLYMER CYLINDER-NANOROD SELF-ASSEMBLY

Boris Rasin

A DISSERTATION

in

Materials Science and Engineering

Presented to the Faculties of the University of Pennsylvania

in

Partial Fulfillment of the Requirements for the

Degree of Doctor of Philosophy

2019

Supervisor of Dissertation

_____

Russell J. Composto

Professor of Materials Science and Engineering, University of Pennsylvania

Graduate Group Chairperson

_____

I-Wei Chen, Professor of Materials Science and Engineering, University of Pennsylvania

Dissertation Committee

Christopher B. Murray, Professor of Materials Science and Engineering, University of Pennsylvania

Robert A. Riggleman, Associate Professor of Chemical and Biomolecular Engineering, University of Pennsylvania

Jeffrey S. Meth, E. I. du Pont de Nemours & Co.

VERTICAL BLOCK COPOLYMER CYLINDER-NANOROD SELF-ASSEMBLY

ACKNOWLEDGMENT

My advisor Russ has been an amazing mentor throughout the course of my PhD. Russ always has excellent scientific advice and insight for my research. By example, Russ also taught me an immense amount about leadership and mentorship. I will always be grateful that Russ gave me freedom to explore, because of this I learned so much. I am most thankful to Russ for his support on good days and bad days, I will always remember this with gratitude.

I would also like to thank my thesis committee. Chris always had great scientific ideas for me and let me use the instruments in his lab. Chris, his group and I collaborated on work presented in this thesis. I worked with Rob extensively during my PhD and every time I met with him I learned so much. I collaborated with him and his group on the work in this thesis, it was fruitful and enriching. Jeff provided insightful advice about my projects and was an amazing mentor. I also collaborated with Jeff on the work in this thesis.

Beyond my thesis committee I had other amazing collaborators during my time at Penn. Benjamin Lindsay and Huikuan Chao were instrumental to the work in this thesis. Xingchen Ye and Benjamin Diroll in Chris' group were great collaborators. Amalie Frischknecht and Christina Ting at Sandia National Laboratories were great to work with. I also collaborated with Nadia Krook. Nadia and I worked on the same research topic during our PhDs. Working with Nadia was excellent and she is a superb scientist. Nadia is also an amazing friend. I would also like to acknowledge the excellent undergraduate students I worked with, Lindsay Tsai and Sona Dadhania.

I would like to acknowledge the members of the Composto group during my time at Penn: Hyun-Su Lee, Emmabeth Parrish, Nadia Krook, Chia-Chun Lin, Sarah Seeger, Robert Ferrier, Naoto Iwata, Jihoon Choi, M. Carme Coll Ferrer, Yuanchi Ma, Daniel Strickland, Benjamin Lindsay, Matthew Caporizzo, Prathima Nalam, Theodore Kurkoski, Carlos Medina, Michael Boyle, Shawn Maguire, Zhengdong Wu, Katie Rose, Alexander Grun, Molly Shave, Connor Bilchak, Christopher O'Bryan, and Xuanbo Liu. I would also like to acknowledge the members of the Winey group during my time at Penn.

I would like to thank Hyun-Su Lee, Eric Bailey, Philip Griffin and Edward Trigg for highly enjoyable scientific discussions and friendship. I would like to thank Ana Alvarez for friendship.

I would also like to acknowledge Matt Brukman (Scanning and Local Probe Facility), Jamie Ford (Nanoscale Characterization Facility), and Douglas Yates (Nanoscale Characterization Facility). I would like to acknowledge Steve Szewczyk for all the help over the years and letting me use/borrow his equipment.

I would like to acknowledge Pat Overend, Vicky Lee, Irene Clements and Enrique Vargas for friendship and for all the help during my time at Penn.

Most importantly I would like to thank my family.

ABSTRACT

VERTICAL BLOCK COPOLYMER CYLINDER-NANOROD SELF-ASSEMBLY

Boris Rasin

Russell J. Composto

The properties of polymer nanocomposites (PNCs) depend on the position and orientation of nanoparticles in the polymer matrix. Improved control over nanoparticle position and orientation in PNCs would result in PNCs with improved properties. A powerful approach to controlling nanoparticle position and orientation in PNCs is nanoparticle-block copolymer (NP-BCP) self-assembly. NP-BCP self-assembly with spherical nanoparticles has been extensively studied. However, NP-BCP self-assembly with anisotropic nanoparticles is less well understood. In this work we study the position and orientation of nanorods in self-assembled nanorod-BCP nanocomposite films. More specifically we study films consisting of polystyrene-*block*-poly(2-vinylpyridine) (PS-*b*-P2VP) and gold nanorods (AuNRs) functionalized with P2VP. When the films are solvent annealed the PS-b-P2VP assumes a morphology of vertical P2VP cylinders in a PS matrix. Relatively short AuNRs are found to localize at the base of the vertical P2VP cylinders with their axis parallel to the substrate. Simulations showed that the AuNRs relieved chain stretching at the base of the cylinders. Studies were done with longer 70 nm and 101 nm long nanorods. The 70 nm nanorods were distributed between three states at the film surface. The three states were the bridging state, the centered state and the vertical state. The bridging state is where the AuNR is embedded in the film surface, the AuNR long axis is parallel to the film surface and each end of the AuNR is at the top of

nearest neighbor P2VP cylinders. The centered state is where the AuNR is embedded in the film surface, the AuNR axis is parallel to the film surface, and the AuNR is centered over a single vertical P2VP cylinder. The vertical state is where the AuNR is localized within a vertical P2VP cylinder, is vertically oriented and has its tip at the film surface. The 101 nm long AuNRs were distributed between the bridging and vertical states at the film surface. The experimental results were compared to hybrid particle-field theory (HPFT) calculations of the system free energy. Further, HPFT simulations were used to understand the block copolymer morphology when a 101 nm long AuNR was in the bridging state.

TABLE OF CONTENTS

LIST OF ILLUSTRATIONS

CHAPTER 1: Introduction

1.1 Background

Polymer nanocomposites (PNCs) consist of a polymer matrix containing nanoparticles. PNCs are very promising materials as incorporating nanoparticles into a polymer can lead to the resultant composite material having improved properties relative to the neat polymer (*e.g*, mechanical properties[1]). Further, the composite material can have properties not present in the neat polymer (*e.g.*, response to a stimulus[2]). Alternatively, PNCs can be viewed as a promising route to taking advantage of the unique properties of the large and growing array of nanoparticles that have been synthesized.[3-5]

The properties of PNCs depend on the position and orientation of the nanoparticles in the polymer matrix. For example, if gold nanorods (AuNRs) are dispersed in a polymer film, the film's optical properties are different than if they are aggregated.[6] One could also envision that if metal nanoparticles could be positioned in a polymer matrix such that they formed a chain of separated nanoparticles this would be a means of fabricating nanoparticle chain waveguides.[7]

Nanoparticle-block copolymer self-assembly is a powerful and versatile approach to control nanoparticle position and orientation in a polymer matrix.[8-9] Block copolymers are polymers consisting of chemically distinct polymers (blocks) (Figure 1.1).

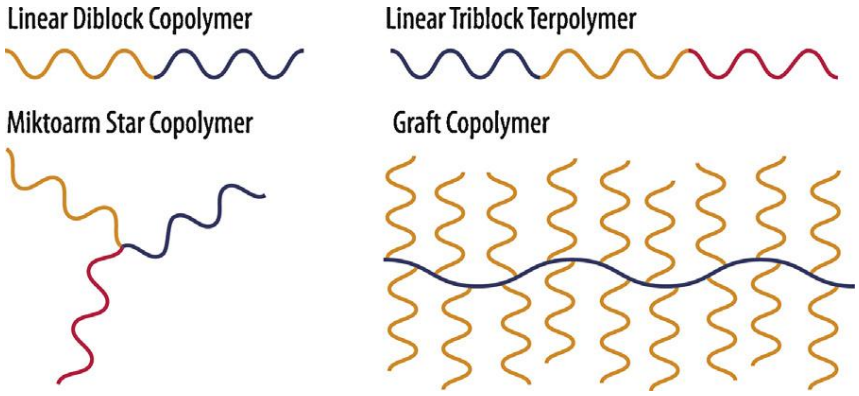

Figure 1.1. Structure of different types of BCPs. Figure reproduced from Hoheisel *et al.*[10]

Going forward we will only consider linear A-B diblock copolymers as this is the block copolymer architecture used in this thesis. Linear A-B diblock copolymers consist of a chain of polymer A bound at the end to a chain of polymer B (Figure 1.1). The strength of segregation between the two blocks in a BCP melt depends on χN, the product of the Flory-Huggins interaction parameter (χ) and the degree of polymerization of the BCP (N).[11] The structure assumed by a linear diblock copolymer depends on χN and the volume fraction of one of the blocks, f (Figure 1.2).[10-11] At a given f, if χN is low enough the BCP will be disordered.[10-11] If χN is increased sufficiently the BCP microphase separates into an ordered morphology.[10-11] Thus, depending on χN and f the BCP assumes a spherical, cylindrical, gyroid, or lamellar morphology.[10-12]

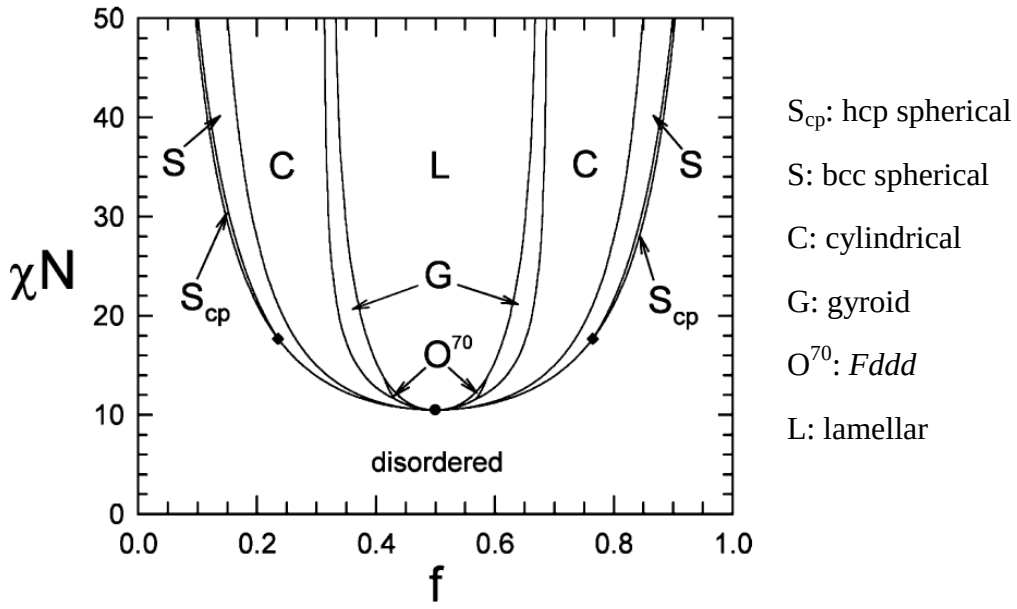

Figure 1.2. A-B diblock copolymer phase diagram calculated from self-consistent field theory. Figure reproduced from Matsen.[12]

Nanoparticle-block copolymer self-assembly is implemented by solvent or thermal annealing a PNC consisting of nanoparticles (NPs) in a BCP matrix. Generally, the goal for self-assembly is as follows. The NPs in the BCP are functionalized such that they have a neutral or favorable enthalpic interaction with one of the blocks and an unfavorable enthalpic interaction with the other block. Upon annealing the BCP will form one of the BCP morphologies described earlier. Simultaneously, the NPs localize in the domains formed by the block with which the NPs have a neutral or favorable enthalpic interaction with. The localization of the NPs in specific domains is used to control their position and orientation.

The thermodynamic contributions which determine the BCP nanocomposite structure are the BCP chain conformational entropy, the NP ligand conformational entropy, the NP translational entropy, the NP orientational entropy, the enthalpic interaction between the two blocks, the enthalpic interaction between the nanoparticle and each block, the enthalpic interaction between the substrate and each block, the enthalpic interaction between the substrate and the NP ligand, the enthalpic interaction between air and each block, and the enthalpic interaction between air and the ligand on the NP.[9, 13-14] Further, if, for example, a nanorod has a permanent dipole moment it will drive nanorod aggregation *via* dipole-dipole coupling.[15]

Much success has been achieved in the localization of NPs in specific BCP domains.[8] However, the full picture is much more nuanced than simply the localization of NPs in specific domains to control NP position and orientation. NPs can affect the morphology of the BCP. For example, NPs can localize at the interface between domains and if their concentration becomes sufficiently high induce a transition from a lamellar to a bicontinuous morphology.[16] NPs can also affect the BCP morphology by causing decreasing grain size with increasing NP concentration.[13] Further, NPs have been shown to affect the types of grain boundaries present in a BCP.[17] Conversely, the same study showed that NPs can localize at grain boundaries.[17] Krook *et al.* showed that when the nanoplate volume fraction in a lamellar nanocomposite becomes sufficiently high lamellae do not form.[18]

NP behavior when localized in BCP domains is also complex. For example, it has been shown that NP position in a lamellar domain depends on the ratio of NP diameter to the domain width and also on NP concentration.[19] Listak *et al.* showed that PS

functionalized gold nanoparticles aggregated in the PS domains of lamellar polyisoprene-*block*-polystyrene-*block*-polyisoprene but were dispersed in the PS domains of lamellar polystyrene-*block*-polyisoprene-*block*-polystyrene.[20] Deshmukh *et al.* showed that nanorods localized in lamellar domains did not assume all orientations allowed by the width of the domain with equal probability.[21] Instead due to the conformational entropy penalty associated with the nanorod being tilted away from parallel to the lamellae plane, the angle between the nanorods and the lamellae plane was tightly distributed around 0^{o}.[21]

1.2 Dissertation Outline

The objective of this thesis is to understand the polymer physics underlying the position and orientation of nanorods in vertical cylinder diblock copolymer films. Films of polystyrene-*block*-poly(2-vinylpyridine) (PS-*b*-P2VP) and AuNRs functionalized with a short P2VP brush were prepared and solvent annealed. Upon solvent annealing the PS-*b*-P2VP assumes a morphology of vertical P2VP cylinders in a PS matrix. Experiments were guided by and compared to simulations. This work advances the field as the studies in this thesis are to our knowledge the first examples of the self-assembly of **vertical** block copolymer morphologies with **anisotropic** nanoparticles. The effect of nanorod dimensions is studied. Further, in this work we find that the AuNRs do not simply localize in the P2VP cylinders with their long axis parallel to the cylinder axis. For the shortest AuNRs studied the nanorods assume a different well defined state, while for the intermediate and long AuNRs studied while vertically oriented AuNRs localized within vertical P2VP cylinders are observed at the film surface, this state is in coexistence with

other well defined states. Our studies of this complex behavior improve the understanding of the complex behaviors that can arise in BCP-NP nanocomposites.

Chapter 2 is a review of the literature on anisotropic NP-BCP self-assembly. Literature on the self-assembly of nanorods and nanoplates with BCPs is reviewed. In Chapter 3 the position and orientation of relatively short AuNRs functionalized with P2VP in vertical cylinder PS-*b*-P2VP nanocomposites is studied. Experiments reveal that the AuNRs are localized at the base of the vertical P2VP cylinders and are oriented parallel to the substrate. Simulations suggest that the AuNRs localize at the base of the vertical P2VP cylinders to relieve chain stretching. Simulations also predict that longer AuNRs will localize in vertical P2VP cylinders and will be vertically oriented. In Chapter 4 the position and orientation of relatively longer AuNRs functionalized with P2VP in vertical cylinder PS-b-P2VP films is studied. Two sizes of nanorods are used, 101 nm in length and 70 nm in length. The 70 nm nanorods are much longer than the nanorods in Chapter 3. Also, the PS-*b*-P2VP films in Chapter 4 are much thicker. We find that the 101 nm nanorods are found in two states at the surface of the vertical cylinder films, the bridging state and the vertical state. The 70 nm nanorods are found in the bridging, centered and vertical states at the surface of the films. Experimental results are compared with system free energies calculated with HPFT simulations. Further, the BCP morphology when a 101 nm nanorod is in the bridging state is calculated with HPFT simulations. In Chapter 5 we describe the conclusions of this thesis and future work. Appendix A contains additional figures and information for Chapter 4.

1.3 References

1. Midya, J.; Cang, Y.; Egorov, S. A.; Matyjaszewski, K.; Bockstaller, M. R.; Nikoubashman, A.; Fytas, G., Disentangling the Role of Chain Conformation on the Mechanics of Polymer Tethered Particle Materials. *Nano Lett* **2019,** *19* (4), 2715-2722.

2. Capadona, J. R.; Shanmuganathan, K.; Tyler, D. J.; Rowan, S. J.; Weder, C., Stimuli-Responsive Polymer Nanocomposites Inspired by the Sea Cucumber Dermis. *Science* **2008,** *319* (5868), 1370-1374.

3. Lohse, S. E.; Burrows, N. D.; Scarabelli, L.; Liz-Marzan, L. M.; Murphy, C. J., Anisotropic Noble Metal Nanocrystal Growth: The Role of Halides. *Chem Mater* **2014,** *26* (1), 34-43.

4. Haase, M.; Schafer, H., Upconverting Nanoparticles. *Angew Chem Int Edit* **2011,** *50* (26), 5808-5829.

5. Smith, A. M.; Nie, S. M., Semiconductor Nanocrystals: Structure, Properties, and Band Gap Engineering. *Accounts Chem Res* **2010,** *43* (2), 190-200.

6. Hore, M. J. A.; Frischknecht, A. L.; Composto, R. J., Nanorod Assemblies in Polymer Films and Their Dispersion-Dependent Optical Properties. *Acs Macro Lett* **2012,** *1* (1), 115-121.

7. Maier, S. A.; Kik, P. G.; Atwater, H. A.; Meltzer, S.; Harel, E.; Koel, B. E.; Requicha, A. A. G., Local Detection of Electromagnetic Energy Transport Below the Diffraction Limit in Metal Nanoparticle Plasmon Waveguides. *Nat Mater* **2003,** *2* (4), 229-232.

8. Kao, J.; Thorkelsson, K.; Bai, P.; Rancatore, B. J.; Xu, T., Toward Functional Nanocomposites: Taking the Best of Nanoparticles, Polymers, and Small Molecules. *Chem Soc Rev* **2013,** *42* (7), 2654-2678.

9. Bockstaller, M. R.; Mickiewicz, R. A.; Thomas, E. L., Block Copolymer Nanocomposites: Perspectives for Tailored Functional Materials. *Adv Mater* **2005,** *17* (11), 1331-1349.

10. Hoheisel, T. N.; Hur, K.; Wiesner, U. B., Block Copolymer-Nanoparticle Hybrid Self-Assembly Preface. *Prog Polym Sci* **2015,** *40*, 3-32.

11. Hamley, I. W., *The Physics of Block Copolymers*. Oxford University Press: Oxford ; New York, 1998; p viii, 424 p.

12. Matsen, M. W., Effect of Architecture on the Phase Behavior of Ab-Type Block Copolymer Melts. *Macromolecules* **2012,** *45* (4), 2161-2165.

13. Thorkelsson, K.; Nelson, J. H.; Alivisatos, A. P.; Xu, T., End-to-End Alignment of Nanorods in Thin Films. *Nano Lett* **2013,** *13* (10), 4908-4913.

14. Lee, J. Y.; Shou, Z.; Balazs, A. C., Modeling the Self-Assembly of Copolymer-Nanoparticle Mixtures Confined between Solid Surfaces. *Phys Rev Lett* **2003,** *91* (13), 136103.

15. Thorkelsson, K.; Mastroianni, A. J.; Ercius, P.; Xu, T., Direct Nanorod Assembly Using Block Copolymer-Based Supramolecules. *Nano Lett* **2012,** *12* (1), 498-504.

16. Kim, B. J.; Fredrickson, G. H.; Hawker, C. J.; Kramer, E. J., Nanoparticle Surfactants as a Route to Bicontinuous Block Copolymer Morphologies. *Langmuir* **2007,** *23* (14), 7804-7809.

17. Listak, J.; Bockstaller, M. R., Stabilization of Grain Boundary Morphologies in Lamellar Block Copolymer/Nanoparticle Blends. *Macromolecules* **2006,** *39* (17), 5820-5825.

18. Krook, N. M.; Ford, J.; Marechal, M.; Rannou, P.; Meth, J. S.; Murray, C. B.; Composto, R. J., Alignment of Nanoplates in Lamellar Diblock Copolymer Domains and the Effect of Particle Volume Fraction on Phase Behavior. *Acs Macro Lett* **2018,** *7* (12), 1400-1407.

19. Chiu, J. J.; Kim, B. J.; Yi, G. R.; Bang, J.; Kramer, E. J.; Pine, D. J., Distribution of Nanoparticles in Lamellar Domains of Block Copolymers. *Macromolecules* **2007,** *40* (9), 3361-3365.

20. Listak, J.; Hakem, I. F.; Ryu, H. J.; Rangou, S.; Politakos, N.; Misichronis, K.; Avgeropoulos, A.; Bockstaller, M. R., Effect of Chain Architecture on the Compatibility of Block Copolymer/Nanoparticle Blends. *Macromolecules* **2009,** *42* (15), 5766-5773.

21. Deshmukh, R. D.; Liu, Y.; Composto, R. J., Two-Dimensional Confinement of Nanorods in Block Copolymer Domains. *Nano Lett* **2007,** *7* (12), 3662-3668.

CHAPTER 2: Anisotropic Nanoparticle-Block Copolymer Self-Assembly

2.1 Introduction

Many aspects of the self-assembly of block copolymers (BCPs) and spherical nanoparticles have been studied.[1-2] Examples of aspects of spherical nanoparticle-BCP self-assembly that have been examined are nanoparticle size[3-4], nanoparticle concentration[3], block copolymer architecture[5], the interaction between nanoparticles and defects[6], specific nanoparticle ligand-block interactions[7], and nanoparticle ligand surface energy[8]. The self-assembly of anisotropic nanoparticles with block copolymers has been less studied but is a growing area of research. Here we review studies of nanorod-block copolymer self-assembly and nanoplate-block copolymer self assembly.

2.2 Review of Nanorod-Block Copolymer Nanocomposites

Deshmukh *et al.* studied lamellar polystyrene-*block*-poly(methyl methacrylate) (PS-*b*-PMMA) films containing polyethylene glycol functionalized gold nanorods.[9] The gold nanorods had a diameter of 12.6 nm and a length of 42.1 nm. The polyethylene glycol ligands on the gold nanorods had a molecular weight of 5000 g/mol. The molecular weight of the PS-*b*-PMMA was M_w = 211,000 g/mol. Nanocomposite films were processed *via* solvent annealing. The solvent annealed films had a lamellar morphology with the lamellae parallel to the substrate. The polyethylene glycol

functionalized gold nanorods were found to be localized in the PMMA lamallae and oriented parallel to the lamellae plane (Figure 2.1). Furthermore, it was found that the AuNRs were aligned to a greater extent than would be expected if they were simply restricted by the dimensions of the PMMA domain. It was proposed that the conformational entropy penalty associated with the nanorod being tilted away from alignment was the cause of the extent of nanorod alignment.

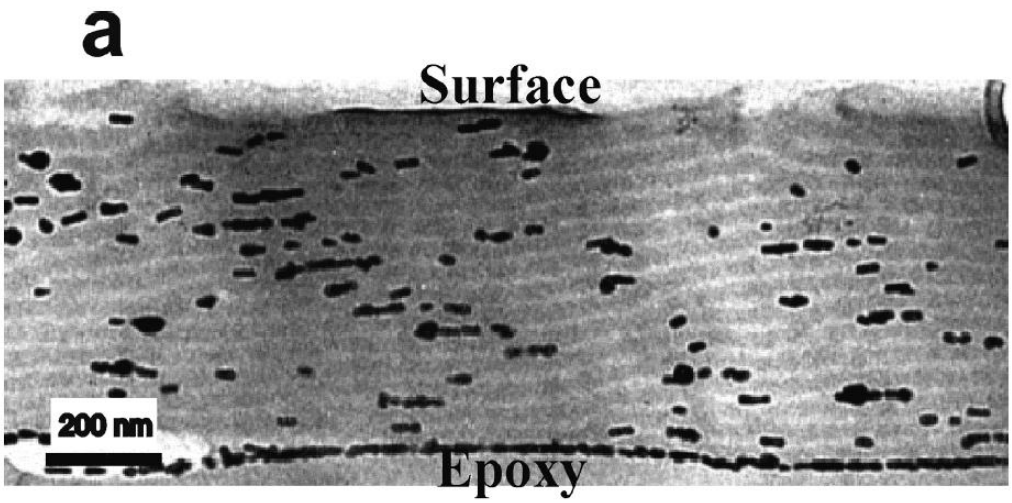

Figure 2.1. A lamellar PS-*b*-PMMA film with the lamellae parallel to the substrate and polyethylene glycol functionalized gold nanorods localized within the PMMA domains and aligned parallel to the domains. Figure reproduced from Deshmukh *et al.*[9]

Thorkelsson *et al.* studied bulk nanocomposites of polystyrene-*b*-poly(4-vinylpyridine)(3-pentadecylphenol)$_n$ (PS-*b*-P4VP(PDP)$_n$) and NRs.[10] *n* is the number of PDP molecules divided by the number of pyridine groups. PDP molecules hydrogen bond to the pyridine groups on the P4VP chain resulting in the formation of a supramolecular coil-comb BCP. Two different NRs were used. The first was CdS NRs with dimensions

of ~ 3-4 nm × 32 nm and a NR-NR interaction of 223 meV when the NRs are positioned side-to-side (a nm × b nm indicates a nanorod with a diameter of a nm and a length of b nm). The second type of NR used was CdSe NRs with dimensions of ~ 3 nm × 25 nm and a NR-NR interaction of 30 meV when the NRs are positioned side-to-side. The ligands on both the CdS and CdSe NRs were alkylphosphonic acids. Nanocomposites were prepared by the slow evaporation of a PS-*b*-P4VP(PDP)$_n$/NR solution. Nanocomposites consisting of PS(40,000 g/mol)-*b*-P4VP(5600 g/mol)(PDP)$_1$, which has a lamellar morphology, and CdSe nanorods were studied. The CdSe NRs were located in the P4VP(PDP)$_1$ domains and had random orientations. Nanocomposites consisting of the lamellar PS(40,000 g/mol)-*b*-P4VP(5600 g/mol)(PDP)$_1$ and CdS NRs were studied. The NRs were found to form rafts that were located at the center of P4VP(PDP)$_1$ domains. Nanocomposites of PS(19,000 g/mol)-*b*-P4VP(5200 g/mol)(PDP)$_3$, which has a morphology of PS cylinders in a P4VP(PDP)$_3$ matrix, and CdS NRs were studied (Figure 2.2a). The CdS NRs were located in the P4VP(PDP)$_3$ matrix, were oriented parallel to the PS cylinders, and were positioned at the interstices in between the PS cylinders (Figure 2.2b). Nanocomposites of PS(116,000 g/mol)-*b*-P4VP(4,000 g/mol)(PDP)$_3$ and CdS NRs were studied. Nanocomposites of PS(116,000 g/mol)-*b*-P4VP(4,000 g/mol)(PDP)$_2$ and CdS NRs were studied as well. The supramolecule for these two nanocomposites has a morphology of P4VP(PDP)$_n$ cylinders in a PS-rich matrix. NRs were localized in the P4VP(PDP)$_n$ cylinders forming tilted and twisted rafts. Nanocomposites of PS(116,000 g/mol)-*b*-P4VP(4,000 g/mol)(PDP)$_1$, which forms a morphology of P4VP(PDP)$_1$ spheres in a PS matrix, and NRs were also studied. Both CdS NR and CdSe NR nanocomposites were studied for this supramolecule.

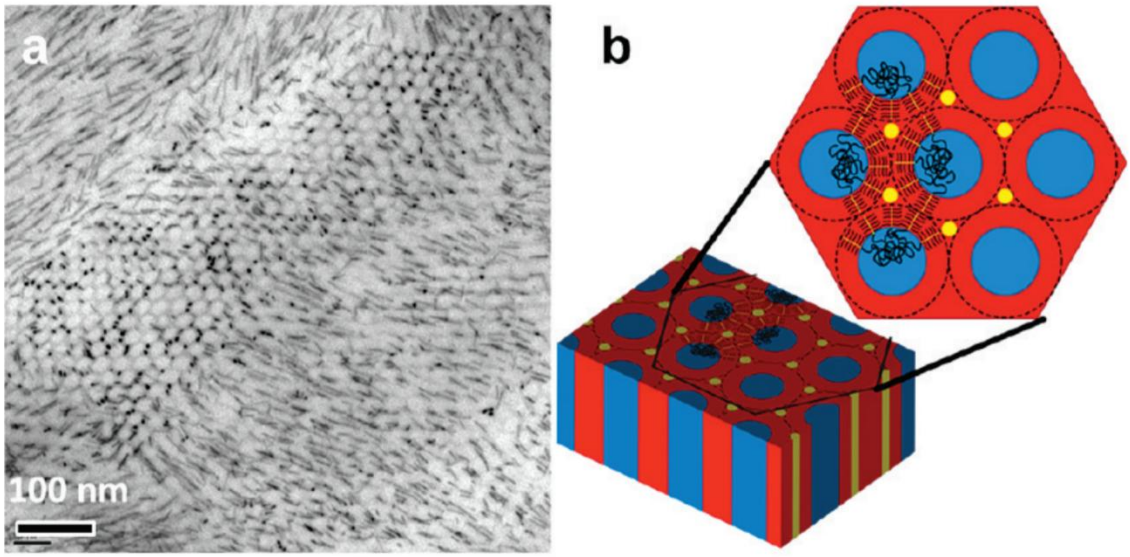

Figure 2.2. (a) TEM image of a PS-b-P4VP(PDP)$_n$ nanocomposite with a supramolecule morphology of PS cylinders in a P4VP(PDP)$_n$ matrix containing CdS nanorods. (b) Diagram of the nanocomposite system. Figure reproduced from Thorkelsson *et al.*[10]

In a different study, Thorkelsson *et al.* studied thin PS(19,000 g/mol)-*b*-P4VP(5200 g/mol)(PDP)$_{1.7}$ films containing NRs.[11] The structure of nanocomposite films containing either 4.5 nm × 20 nm CdSe/CdS seeded NRs, 6.0 nm × 40 nm CdSe/CdS seeded NRs, or 4.8 nm × 60 nm CdS NRs was examined. The ligands on the NRs were alkylphosphonic acids. For each of the three NRs the volume fraction of NRs in the film was varied from 1% to 10%. Nanocomposite films were processed by solvent annealing and the PS-b-P4VP(PDP)$_{1.7}$ had a morphology of PS cylinders in a P4VP(PDP)$_{1.7}$ matrix. When the shortest NRs, the 20 nm long NRs, were incorporated into the supramolecule at a volume fraction of 10% it was found that the NRs were localized within the

P4VP(PDP)$_{1.7}$ matrix at a variety of angles between the NR long axis and the adjacent PS cylinders. It was also found that the NR volume fraction did not substantially affect grain size. For the 40 nm long NRs, at volume fractions of 1%, 3% and 6% NRs were located in the P4VP(PDP)$_{1.7}$ matrix with their long axis parallel to the adjacent PS cylinders. At a volume fraction of 3% NRs were positioned end-to-end in the P4VP(PDP)$_{1.7}$ matrix. When the volume fraction was increased to 10% NRs were positioned side-to-side. Further, it was found that grain size decreased with increasing NR volume fraction. At volume fractions of 1% and 3%, the longest NRs, the 60nm NRs, were localized within the P4VP(PDP)$_{1.7}$ matrix and their long axis was parallel to the adjacent PS cylinders. Further, at a volume fraction of 3% the NRs were positioned end-to-end. At volume fractions of 6% and 10% NRs were positioned side-to-side. Grain size was found to decrease as NR volume fraction was increased.

Ploshnik *et al.* studied thin nanocomposite films consisting of PS-*b*-PMMA and CdSe NRs.[12] The PS-*b*-PMMA had M_n = 895,000 g/mol with a PS wt % of 29.6. The PS-*b*-PMMA had a morphology of PS cylinders in a PMMA matrix. CdSe NRs were functionalized with thiol terminated polystyrene. The thiol terminated PS had M_n = 2600 g/mol or M_n = 3500 g/mol. CdSe NRs of the following dimensions were used: 4.6 nm × 33 nm, 3.8 nm × 21 nm, 3.9 nm × 11 nm. The nanocomposite thin films were spin-coated from solutions consisting of PS-*b*-PMMA and PS functionalized CdSe NRs in toluene on hydrophilic silicon wafers. The nanocomposite thin films were processed *via* solvent annealing in chloroform. Nanocomposite PS-*b*-PMMA films containing 4.6 nm × 33 nm CdSe NRs that were spin-coated from .25 PS-*b*-PMMA wt % solutions were studied

(Figure 2.3). The nanocomposite films had an NR volume fraction of .36 and were 10 nm-20 nm thick. The nanocomposite films had a PS-*b*-PMMA morphology that could be interpreted as either parallel cylinders or vertical lamellae. CdSe NRs were observed at the surface of PS domains and were parallel to the surface. The long axis of the CdSe NRs was perpendicular to the axis of the PS domain. Nanocomposites prepared with a volume fraction of 0.20 of 3.8 nm × 21 nm CdSe NRs and nanocomposites prepared with a volume fraction of 0.15 of 3.9 nm × 11 nm CdSe NRs were also studied. For the 3.9 nm × 11 nm NRs, the NRs were found to assume a variety of angles relative to the PS domain axis with peaks in the angle distribution near 0º (parallel) and 90º (perpendicular). Nanocomposites consisting of PS-*b*-PMMA with a volume fraction of 0.36 of 4.6 nm × 33 nm CdSe NRs were spin-coated from 0.50 PS-*b*-PMMA wt % solutions. The 4.6 nm × 33 nm NR nanocomposites described earlier had the same volume fraction of NRs but were spin-coated from 0.25 PS-*b*-PMMA wt % solutions. The 4.6 nm × 33 nm NR PS-*b*-PMMA nanocomposites spin-coated from the 0.50 PS-b-PMMA wt % solutions had a film thickness of 30 nm. The NRs in these nanocomposites formed three dimensional aggregates.

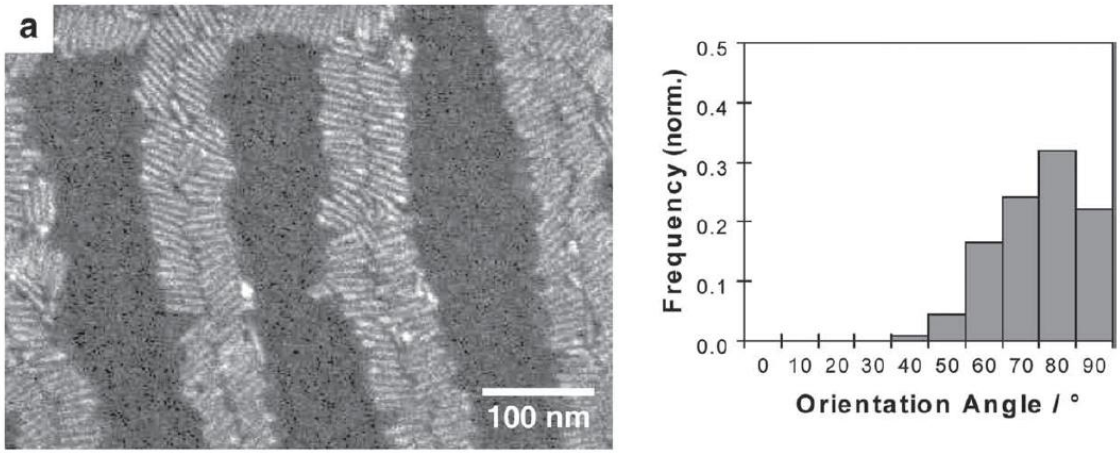

Figure 2.3. (Left) SEM image of a PS-*b*-PMMA nanocomposite film containing a volume fraction of 0.36 of 4.6 nm × 33 nm CdSe NRs and spin-coated from a 0.25 PS-*b*-PMMA wt % solution. (Right) Histogram of angles between the nanorod long axis and the PS domain axis. Figure reproduced from Ploshnik *et al.*[12]

2.3 Review of Nanoplate-Block Copolymer Nanocomposites

Krook *et al.* studied nanocomposite films consisting of PS-*b*-PMMA and GdF_3:Yb/Er (20/2 mol %) nanoplates.[13] The nanoplates were rhombic with dimensions 22 nm (diagonal 1) by 35 nm (diagonal 2) by 3 nm (thickness). The nanoplates were functionalized with phosphoric acid terminated polyethylene glycol (M_n = 5000 g/mol). The PS-*b*-PMMA had M_n = 38,000 g/mol-*b*-36,800 g/mol and a lamellar morphology. Nanocomposite films were processed *via* thermal annealing at 190 ºC. The volume fraction of nanoplates was varied. Nanoplates were found to localize in PMMA lamellae and were aligned for the lowest nanoplate volume fractions (Figure 2.4). When the nanoplate volume fraction was increased regions where the lamellar morphology formed but no nanoplates were present were observed. In other regions nanoplates were present but no lamellar formation was observed. When the nanoplate volume fraction was

increased further, the lamellar morphology was not observed and nanoplates were unaligned.

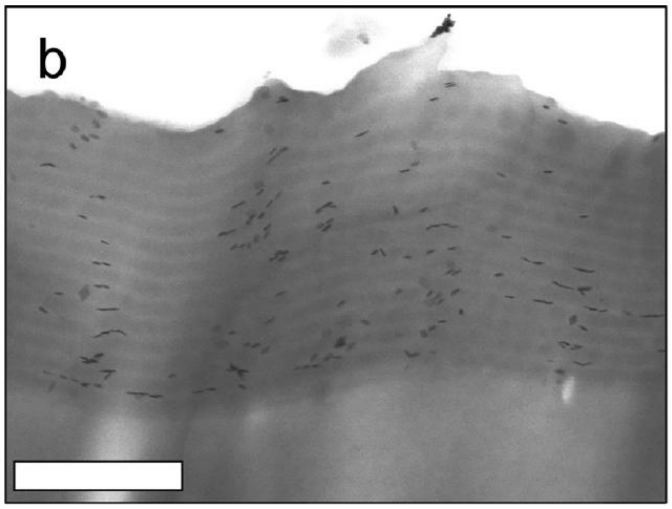

Figure 2.4. TEM image of a PS-*b*-PMMA lamellar film containing GdF_3:Yb/Er (20/2 mol %) nanoplates functionalized with polyethylene glycol. The nanoplates are localized within the PMMA domains and aligned. The volume fraction of nanoplates is 0.017. Figure reproduced from Krook *et al.*[13]

2.4 Conclusions

Additional papers of interest can be found in the following references: nanorods[14-15], nanoplates[16]. A potential future direction for anisotropic NP-BCP self-assembly is to develop methods of increasing anisotropic NP volume fraction without preventing the BCP from ordering or substantially reducing the BCP grain size. Another interesting future direction is studying anisotropic NP localization at the interface between domains. The localization of spherical NPs at the interface between domains has been studied extensively. On the other hand there are no current studies on anisotropic nanoparticle

localization at the interface between BCP domains. Lastly, the studies of anisotropic nanoparticle BCP self-assembly that have been conducted all use linear diblock copolymers or linear diblock copolymer-like supramolecules. Exploring the self-assembly of anisotropic nanoparticles with block copolymers of other architectures could lead to a better understanding of anisotropic NP-BCP self assembly and to improved nanocomposite materials.

2.5 References

1. Kao, J.; Thorkelsson, K.; Bai, P.; Rancatore, B. J.; Xu, T., Toward Functional Nanocomposites: Taking the Best of Nanoparticles, Polymers, and Small Molecules. *Chem Soc Rev* **2013,** *42* (7), 2654-2678.

2. Sarkar, B.; Alexandridis, P., Block Copolymer-Nanoparticle Composites: Structure, Functional Properties, and Processing. *Prog Polym Sci* **2015,** *40*, 33-62.

3. Chiu, J. J.; Kim, B. J.; Yi, G. R.; Bang, J.; Kramer, E. J.; Pine, D. J., Distribution of Nanoparticles in Lamellar Domains of Block Copolymers. *Macromolecules* **2007,** *40* (9), 3361-3365.

4. Bockstaller, M. R.; Lapetnikov, Y.; Margel, S.; Thomas, E. L., Size-Selective Organization of Enthalpic Compatibilized Nanocrystals in Ternary Block Copolymer/Particle Mixtures. *J Am Chem Soc* **2003,** *125* (18), 5276-5277.

5. Listak, J.; Hakem, I. F.; Ryu, H. J.; Rangou, S.; Politakos, N.; Misichronis, K.; Avgeropoulos, A.; Bockstaller, M. R., Effect of Chain Architecture on the Compatibility of Block Copolymer/Nanoparticle Blends. *Macromolecules* **2009,** *42* (15), 5766-5773.

6. Listak, J.; Bockstaller, M. R., Stabilization of Grain Boundary Morphologies in Lamellar Block Copolymer/Nanoparticle Blends. *Macromolecules* **2006,** *39* (17), 5820-5825.

7. Lin, Y.; Daga, V. K.; Anderson, E. R.; Gido, S. P.; Watkins, J. J., Nanoparticle-Driven Assembly of Block Copolymers: A Simple Route to Ordered Hybrid Materials. *J Am Chem Soc* **2011,** *133* (17), 6513-6516.

8. Lin, Y.; Boker, A.; He, J. B.; Sill, K.; Xiang, H. Q.; Abetz, C.; Li, X. F.; Wang, J.; Emrick, T.; Long, S.; Wang, Q.; Balazs, A.; Russell, T. P., Self-Directed Self-Assembly of Nanoparticle/Copolymer Mixtures. *Nature* **2005,** *434* (7029), 55-59.

9. Deshmukh, R. D.; Liu, Y.; Composto, R. J., Two-Dimensional Confinement of Nanorods in Block Copolymer Domains. *Nano Lett* **2007,** *7* (12), 3662-3668.

10. Thorkelsson, K.; Mastroianni, A. J.; Ercius, P.; Xu, T., Direct Nanorod Assembly Using Block Copolymer-Based Supramolecules. *Nano Lett* **2012,** *12* (1), 498-504.

11. Thorkelsson, K.; Nelson, J. H.; Alivisatos, A. P.; Xu, T., End-to-End Alignment of Nanorods in Thin Films. *Nano Lett* **2013,** *13* (10), 4908-4913.

12. Ploshnik, E.; Salant, A.; Banin, U.; Shenhar, R., Hierarchical Surface Patterns of Nanorods Obtained by Co-Assembly with Block Copolymers in Ultrathin Films. *Adv Mater* **2010,** *22* (25), 2774-2779.

13. Krook, N. M.; Ford, J.; Marechal, M.; Rannou, P.; Meth, J. S.; Murray, C. B.; Composto, R. J., Alignment of Nanoplates in Lamellar Diblock Copolymer Domains and the Effect of Particle Volume Fraction on Phase Behavior. *Acs Macro Lett* **2018,** *7* (12), 1400-1407.

14. Ploshnik, E.; Salant, A.; Banin, U.; Shenhar, R., Co-Assembly of Block Copolymers and Nanorods in Ultrathin Films: Effects of Copolymer Size and Nanorod Filling Fraction. *Phys Chem Chem Phys* **2010,** *12* (38), 11885-11893.

15. Halevi, A.; Halivni, S.; Oded, M.; Muller, A. H. E.; Banin, U.; Shenhar, R., Co-Assembly of a-B Diblock Copolymers with B'-Type Nanoparticles in Thin Films: Effect of Copolymer Composition and Nanoparticle Shape. *Macromolecules* **2014,** *47* (9), 3022-3032.

16. Hsu, S. W.; Xu, T., Tailoring Co-Assembly of Nanodiscs and Block Copolymer-Based Supramolecules by Manipulating Interparticle Interactions. *Macromolecules* **2019,** *52* (7), 2833-2842.

CHAPTER 3: Dispersion and Alignment of Nanorods in Cylindrical Block Copolymer Thin Films

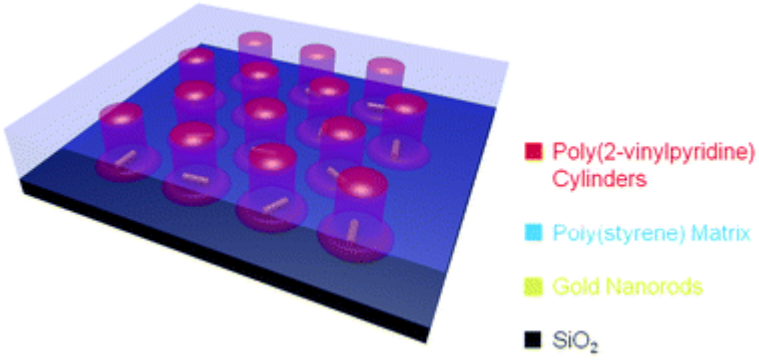

This chapter was published as follows:

Rasin, B.; Chao, H. K.; Jiang, G. Q.; Wang, D. L.; Riggleman, R. A.; Composto, R. J., Dispersion and Alignment of Nanorods in Cylindrical Block Copolymer Thin Films. Soft Matter 2016, 12 (7), 2177-2185.

3.1 Abstract

Although significant progress has been made in controlling the dispersion of spherical nanoparticles in block copolymer thin films, our ability to disperse and control the assembly of anisotropic nanoparticles into well-defined structures is lacking in comparison. Here we use a combination of experiments and field theoretic simulations to examine the assembly of gold nanorods (AuNRs) in a block copolymer. Experimentally, poly(2-

vinylpyridine)-grafted AuNRs (P2VP–AuNRs) are incorporated into poly(styrene)-*b*-poly(2-vinylpyridine) (PS-*b*-P2VP) thin films with a vertical cylinder morphology. At sufficiently low concentrations, the AuNRs disperse in the block copolymer thin film. For these dispersed AuNR systems, atomic force microscopy combined with sequential ultraviolet ozone etching indicates that the P2VP–AuNRs segregate to the base of the P2VP cylinders. Furthermore, top-down transmission electron microscopy imaging shows that the P2VP–AuNRs mainly lie parallel to the substrate. Our field theoretic simulations indicate that the NRs are strongly attracted to the cylinder base where they can relieve the local stretching of the minority block of the copolymer. These simulations also indicate conditions that will drive AuNRs to adopt a vertical orientation, namely by increasing nanorod length and/or reducing the wetting of the short block towards the substrate.

3.2 Introduction

Polymer nanocomposites are versatile hybrid materials utilized in applications ranging from environmental (*e.g.*, light-weighting vehicles) to biomedical (*e.g.*, drug delivery). In part, this versatility originates from the breadth of particle properties, such as optical, electronic and magnetic, and shapes, such as spheres, cubes and rods that are now accessible.[1–5] The coassembly of spherical nanoparticles in block copolymers (BCPs) has been of great interest since the seminal theoretical and experimental studies by Balazs, Thomas, Russell, Kramer, Pine and others.[6–11] Whereas the spatial distribution of spherical nanoparticles in BCPs has received much interest, the full spectrum of heterogeneous materials accessible by combining the versatility of BCP morphology with nanoparticle shape is only beginning to be resolved. In particular, recent studies of anisotropic

nanoparticles, namely nanorods (NRs) in homopolymer[12–16] show that dispersion and alignment can be controlled by grafting brushes to the NR surface resulting in a tunable structure–property (optical) relationship. Presently, the breadth of studies of NR assembly in BCPs is rather limited,[17–29] and in particular interactions between NRs and defects in BCPs have not been explored.

A powerful and versatile approach for ordering NRs in BCP nanocomposites, which we use in this work, is to prepare BCP NR nanocomposites and thermally or solvent anneal them. This approach has been employed extensively in previous work. Composto *et al.* studied the self-assembly of poly(ethylene glycol) (PEG) functionalized gold NRs (AuNRs) in poly(styrene)-*b*-poly(methyl methacrylate) (PS-*b*-PMMA) lamellae.[22] The AuNRs localized in the PMMA domains and were oriented parallel to the lamellar planes. Xu *et al.* studied the self-assembly of alkyl phosphonic acid capped NRs in BCP-based supramolecules.[17,25] The supramolecule was poly(styrene)-*b*-poly(4-vinylpyridine) (3-pentadecylphenol)$_r$ (PS-*b*-P4VP(PDP)$_r$) which has a coil-comb structure and both bulk and thin film nanocomposites were investigated.[17,25] In bulk nanocomposites where the PS-*b*-P4VP(PDP)$_r$ had a morphology of P4VP(PDP)$_r$ cylinders in a PS matrix, NRs were localized within the P4VP(PDP)$_r$ cylinders forming rafts.[25] In nanocomposites where the supramolecule morphology was PS cylinders in a P4VP(PDP)$_r$ matrix, NRs were positioned in the matrix at the interstitial sites between the PS cylinders oriented with their long axes parallel to the PS cylinders.[25] In their study of thin film PS-*b*-P4VP(PDP)$_r$/NR nanocomposites Xu *et al.* investigated the structure of films where the supramolecule had a morphology of PS cylinders parallel to the substrate in a P4VP(PDP)$_r$ matrix.[17] Xu *et*

al. showed that NRs could be aligned end-to-end in the P4VP(PDP)$_r$ matrix parallel to PS cylinders.[17] Banin and Shenhar *et al.* investigated the self-assembly of polystyrene functionalized NRs on thin PS-*b*-PMMA films.[19,26] They showed the selective localization of NRs on top of PS block stripes with the NRs being oriented perpendicular to the PS/PMMA interface.[19,26] Shenhar *et al.* studied the structure of PS-*b*-PMMA nanocomposite films containing PEO functionalized nanospheres and NRs.[24] It was shown that NRs can affect the BCP morphology differently from nanospheres.[24] Lo *et al.* investigated nanocomposites of pyridine functionalized Fe_2P NRs and lamellae forming poly(styrene)-*b*-poly(2-vinylpyridine) (PS-*b*-P2VP).[23,28] In these two studies the effect of NR length, NR concentration and BCP molecular weight on the nanocomposite structure was examined. Using roll casting, Swager and Thomas *et al.* prepared polystyrene-*b*-polyisoprene-*b*-polystyrene films containing PS-grafted poly(*p*-phenylene-ethynylene) that locate in the cylindrical PS domains.[30] The PS cylinders were oriented parallel to the substrate and the PS-grafted poly(*p*-phenylene-ethynylene) molecules were aligned within the cylinders.[30]

Nanoparticles in BCPs can affect microstructure defects. For example, Xu *et al.* showed that nanoparticle volume fraction can affect grain size and Listak and Bockstaller demonstrated that the presence of nanoparticles in a lamellar BCP can increase the fraction of tilt grain boundaries which are T-junction grain boundaries.[17,31] The study by Listak and Bockstaller also showed that NP position can be affected by defects in the microstructure.[31] For example, they showed that NPs aggregate at specific positions of T-junction grain boundaries to relieve chain stretching. Furthermore, Listak and Bockstaller propose that the position of nanoparticles in BCP thin films could be controlled by

introducing high-stress defects at desired positions along the film. In this work NR position and orientation in BCP thin films is determined by defects in vertical BCP cylinders. To our knowledge our study is the first to control the position and orientation of anisotropic nanoparticles in BCPs using microstructure defects.

While there have been several simulation studies of NRs in homopolymers,[32–34] computational and theoretical studies of NR assembly in a BCP have been limited due to the NRs' slow dynamics and the difficulty in equilibrating BCPs using particle-based simulations. Although polymer field theory is an attractive approach to study BCP morphology, including anisotropic nanoparticles in the calculations is computationally demanding, and therefore previous studies have generally been limited to two dimensions. For example, Balazs *et al.* used the self-consistent field theory/density functional theory (SCFT/DFT) approach to simulate a BCP system with nanorods.[35] Their results showed that the distribution of the NRs in the lamellar and cylindrical phases can be controlled by varying NR composition and aspect ratio. However, this study assumed a uniform and static orientation of nanorods, and all simulations were performed using the mean-field approximation. Separately, Tang and Ma used the hybrid particle field theory (HPF) and found that the morphology of the phase separated BCP matrix depends not only on the BCP composition but also the volume fraction and aspect ratio of the NRs.[36]

Recently, we have developed a method to incorporate nanoparticles directly into the field theoretic simulation approach[37–39] using a generic framework that can in principle be applied to any nanoparticle shape. The method is very closely related to the hybrid particle field theory method of Sides *et al.*,[40] but in our approach the nanoparticles are traced through

the particle-to-field transformation along with the polymeric components. Importantly, we do not have to include any additional density functional theory terms in our model to capture correlations between the particles. This allows us to relax the main assumption present in SCFT (the mean-field approximation), which we have shown has implications on the distribution of NRs in a lamellar-forming BCP.[37]

In this manuscript, we use a combination of experiments and field theoretic simulations to examine the location of NRs dispersed in defect-containing, vertically-oriented cylinder forming BCP thin films. Experimentally, we employ P2VP-grafted AuNRs mixed with PS-*b*-P2VP having a P2VP volume fraction of 0.28. Solvent annealing in chloroform is used to create vertically oriented P2VP cylinders in 63 nm films. Because P2VP chains preferentially wet the oxide substrate, defects form near the substrate where the vertical P2VP cylinders transform into a planar wetting layer parallel to the substrate. We find that the P2VP–AuNRs remain well dispersed and form few and small aggregates at a volume fraction of 0.25 vol%. Using ultraviolet ozone (UVO) etching combined with atomic force microscopy (AFM), the location of the NRs are shown to correlate with the P2VP cylinders and locate near the substrate suggesting that the NRs segregate towards the interface. Whereas transmission electron microscopy (TEM) confirms that NRs correlate with the P2VP cylinders, these top-down micrographs also show that a majority of the AuNRs align parallel to the substrate (*i.e.*, perpendicular to the P2VP cylinders) and appear individually or in small aggregates. Using parameters that mimic experiments, field theoretic simulations indicate that a combination of the wetting properties of the substrate and NR geometry both

play a key role in determining the location of the NRs. Furthermore, simulations suggest that vertical orientation of NRs can be achieved by increasing the length of the AuNR.

3.3 Experimental Materials and Methods

The NRs were synthesized with reagents obtained from Sigma Aldrich. Poly(2-vinylpyridine) thiol (P2VP–SH, M_n = 2500 g mol^{-1}) and PS-*b*-P2VP (M_n = 180 kg mol^{-1}-*b*-M_n = 77 kg mol^{-1}) PDI 1.09, volume fraction P2VP 0.283 was purchased from Polymer Source. The seeded growth method was used to synthesize the AuNRs.[41,42] A 40 mL solution of 0.1 M hexadecyltrimethylammonium bromide(CTAB) was prepared and to it was added 1.7 mL of 0.1 M $HAuCl_4 \cdot 3H_2O$, 0.25 mL of $AgNO_3$, 0.27 mL of ascorbic acid, and 0.42 mL of a gold seed solution which was followed by at least 3 hours of incubation at a temperature of 40 °C. The nanorod dimensions were determined with TEM and the average AuNR diameter and length were 7.9 nm and 28.4 nm respectively, an aspect ratio of 3.6. To remove excess CTAB the NR solution was centrifuged two times (30 minutes, 10 000 RPM each time). M_n = 2500 g mol^{-1} P2VP–SH was dissolved in ethanol to prepare a 2 mL 2 mM solution and to it 0.3 mL of highly concentrated AuNRs was added. The resulting solution was stirred for more than 12 hours. The solution was then centrifuged (20 minutes, 10 000 RPM), the supernatant was removed, and the AuNR were moved to methanol. The AuNR in methanol were then centrifuged, the supernatant was removed, and the AuNR were moved to tetrahydrofuran (THF). Only several percent of the synthesized nanoparticles were not nanorods. The grafting density of P2VP–SH on the AuNR was 0.86 chains per nm^2.[14]

Nanocomposite films were prepared on silicon substrates cleaned with Piranha solution (80 °C, 30 min). (**Caution**: Piranha solution is prepared with 30 vol% H_2O_2/70 vol% H_2SO_4 and should be handled with extreme care under fumehood!) 1 wt% solutions of P2VP–AuNR:PS-*b*-P2VP in THF were prepared and spin-coated at 2000–3000 RPM for 60 s. The thin films were dried in a vacuum for 6 hours. The average film thickness was 63 nm as measured with ellipsometry. BCP nanocomposite films with 0.25, 0.8, and 1 volume percent AuNR were prepared.

BCP nanocomposites were characterized with TEM (JEOL JEM 2010 at 200 kV) by picking up nanocomposite films with TEM grids (Electron Microscopy Sciences) after they were floated off the silicon substrates with a pH 10 basic solution. ImageJ was used to determine the number of dispersed individual nanorods.[43] AFM (Picoplus, Agilent Technologies) characterization was done in tapping mode.

3.4 Field Theoretic Simulations

To sample the equilibrium distributions of NRs in a BCP confined between planar walls, we adopt a recent extension of polymer field theory that enables a general study of polymer nanocomposites, which we refer to as polymer nanocomposite field theory, PNC-FT. Here we recount the key details and refer the interested reader to ref. 37 for the complete derivation and demonstration of the method. Our model includes A–B BCPs modeled as discrete Gaussian chains discretized into N interaction sites with a composition $f_A = N_A/N$. Experimentally the AuNRs are highly functionalized with P2VP thiol, which presumably prevents strong NR–NR interactions and allows the P2VP–AuNRs to have an overall neutral

interaction with the P2VP. Therefore, in our field theoretic model, we treat the NRs as chemically identical to the A block of the BCP without explicitly modeling the grafted chains on the surface of the nanorods. In the experiments, the length of the P2VP blocks is much longer than the grafted P2VP chains, and in the thermodynamics of grafted nanoparticles in homopolymers it is known that under these conditions a homopolymer melt can dewet the brush layer, leading to nanoparticle aggregation,[44–46] though recent simulations and experiments challenge the assumed relationship between these phenomena.[47] Our assumption of modeling the nanoparticles as bare nanoparticles and the importance of autophobic dewetting in block copolymers will be addressed in a forthcoming publication.

The interactions between the A and B segments are taken through a standard Flory repulsive potential governed by χ_{AB}, and we assume that our melt is weakly compressible.[48] The energy penalty against density fluctuations away from the average density ρ_0 is taken as

$$\beta U = \frac{\zeta}{2\rho_0}\int \mathrm{d}\mathbf{r}\left(\sum_i \hat{\rho}_i(\mathbf{r}) - \rho_0\right)^2, \tag{1}$$

where ζ controls the compressibility of the system, and the sum over i goes over the A and B blocks of the copolymer, the NRs, and the density profile associated with the confining walls. The density of the wall acts as a cavity function to exclude the polymer segments, and the walls will be used to impart confinement onto our systems.[49] Rather than the standard treatment of the polymer segment densities as point particles, following previous work,[50–52] we use polymer segments that have their mass distributed over unit Gaussians. Importantly, we have shown[37,39] that a similar treatment can be applied to nanoparticles using

the cavity functions commonly employed in the hybrid particle/field theory methods,[38,40] and so the total nanoparticle density is given by $\hat{\rho}_{\mathrm{P}}(\mathbf{r}) = \sum_{i}^{n_{\mathrm{P}}} \Gamma\left(\mathbf{r} - \mathbf{r}_i, \mathbf{u}_i\right)$ where $\Gamma(\mathbf{r}, \mathbf{u})$ is the density distribution function that describes the shape of a NR with orientation **u**. Our choice for $\Gamma(\mathbf{r}, \mathbf{u})$ is given by

$$\Gamma(\mathbf{r},\mathbf{u}) = \frac{\rho_0}{4}\mathrm{erfc}\left[\frac{|\mathbf{r}\cdot\mathbf{u}| - L_{\mathrm{P}}/2}{\xi}\right]\mathrm{erfc}\left[\frac{|\mathbf{r}\times\mathbf{u}| - R_{\mathrm{P}}}{\xi}\right], \tag{2}$$

where L and R are the length and radius of the NR, respectively, and ξ is a numerical parameter that quantifies the range over which the density of the nanoparticle smoothly changes from ρ_0 to 0. The density profiles associated with the confining walls are given by masking functions of the form[49]

$$\hat{\rho}_{\mathrm{W}}(\mathbf{r}) = \frac{\rho_0}{2}\left[1 - \tanh\left(\frac{|z| - L_{\mathrm{w}}}{\xi}\right)\right], \tag{3}$$

where $|z|$ is the distance from **r** in the simulation box to the $z = 0$ plane, corrected for periodic boundary conditions, and L_{w} is the total thickness of the wall. This creates a wall with two surfaces on either side of the simulation box in the z-direction.

The interactions between the polymer segments and the nanoparticles are decoupled using formally exact Hubbard–Stratonovich transformations, which leads to a system with the canonical partition function

$$\mathcal{Z} = z_0 \int \mathcal{D}w_+ \int \mathcal{D}w_- \, \mathrm{e}^{-\mathcal{H}[w_+, w_-]}, \tag{4}$$

where z_0 contains the normalization factors (*e.g.*, the factors of $n!$, the thermal de Broglie wavelength, *etc.*). $\mathcal{H}$ is the effective Hamiltonian of the system, and is given by

$$\mathcal{H}[w_+, w_-] = \frac{\rho_0}{\chi_{AB}} \int d\mathbf{r} [w_-(\mathbf{r})]^2 + \frac{\rho_0}{2\kappa} \int d\mathbf{r} [w_+(\mathbf{r})]^2 - i\rho_0 \int d\mathbf{r} w_+(\mathbf{r}) \\ -n_D \log Q_D[w_A, w_B] - n_R \log Q_R[w_R]. \tag{5}$$

Here, $\kappa = \chi_{AB} + 2\zeta$, Q_D is the partition function of a single BCP chain, and w_A and w_B are the chemical potential fields experienced by the A and B segments of the diblock copolymer, respectively, defined as $w_A = (h * [iw_+ - w_-])(\mathbf{r})$ and $w_B = (h * [iw_+ + w_-])(\mathbf{r})$. Here, the asterisk indicates a convolution and $h(\mathbf{r})$ is a unit Gaussian that distributes the mass of a statistical segment over a finite volume, which serves to both regularize the theory against ultraviolet divergences[50,51] and give positional correlations to the polymer segments.[38] The chemical potential field $w_R(\mathbf{r}, \mathbf{u})$ is the field experienced by the NRs given by

$$w_R(\mathbf{r}, \mathbf{u}) = \int d\mathbf{r}' [iw_+(\mathbf{r}') - w_-(\mathbf{r}')] \Gamma(\mathbf{r} - \mathbf{r}', \mathbf{u}), \tag{6}$$

and we note that the orientation dependence of w_R only arises through the orientation dependence of the density distribution function Γ; there are no specific anisotropic interactions between the NRs.

The single-chain partition function Q_D is calculated as

$$Q_D = \frac{1}{V} \int d\mathbf{r}\, q_D(\mathbf{r}, j = N; [w_A, w_B]), \tag{7}$$

where $q_D(\mathbf{r}, j)$ is the chain propagator, constructed by iterating the Chapman–Kolmogorov equation

$$q_{\mathrm{D}}(r,j) = \mathrm{e}^{-w_{\mathrm{K}}(\mathbf{r})} \int \mathrm{d}\mathbf{r}' \Phi(\mathbf{r}-\mathbf{r}')\, q_{\mathrm{D}}(\mathbf{r}, j-1), \tag{8}$$

subject to the initial condition $q_{\mathrm{D}}(\mathbf{r}, j = 1) = \mathrm{e}^{-w_{\mathrm{A}}(\mathbf{r})}$ and where K is either A or B depending on whether segment j is an A or B segment. In eqn (8), $\Phi(\mathbf{r})$ is the normalized bond transition probability.

Finally, Q_{R} is the NR partition function defined as

$$Q_{\mathrm{R}} = \frac{1}{4\pi V} \int \mathrm{d}\mathbf{u} \int \mathrm{d}\mathbf{r}\, \mathrm{e}^{-w_{\mathrm{R}}(\mathbf{r},\mathbf{u})}, \tag{9}$$

where **u** is a unit vector that points along the length of the NR, and the integral over $\int \mathrm{d}\mathbf{u}$ is over all possible NR orientations.

The theory described here is evaluated at two levels. Most of the results presented below are from sampling the fully-fluctuating field theory using complex Langevin (CL) simulations[53,54] where the fields are evolved according to

$$\frac{\partial w_{\pm}(\mathbf{r})}{\partial t} = -\lambda_{\pm} \frac{\delta \mathcal{H}}{\delta w_{\pm}(\mathbf{r})} + \eta_{\pm}(\mathbf{r}, t), \tag{10}$$

where $\eta(\mathbf{r}, t)$ is a purely real Gaussian white noise term whose statistics are chosen to satisfy the fluctuation dissipation theorem. The CL equations were discretized in time and evolved using a first-order semi-implicit algorithm[55] with a time step of $\lambda_{\pm}\delta t = 10^{-5}$, and our CL results were averaged over 50 000 iterations of eqn (10). We emphasize that the "time" variable in eqn (10) does not represent a physical time, and integrating eqn (10) does not lead to realistic dynamics in our system.

The second level on which we will evaluate our theory will be to study systems containing a single NR where we wish to precisely control its position and orientation. To achieve this, we will adopt the hybrid particle/field theory method[40] with a NR described by the density distribution function given above in eqn (2). The hybrid particle/field theory calculations will treat the chemical potential fields $w_{\pm}$ at the mean-field level, and the mean-field solutions are obtained by evolving eqn (10) without the noise term.

All of the calculations presented below use the simulation parameters $\chi N = 20$, $\kappa N = 40$, $f = N_A/(N_A + N_B) = 0.3$, a polymer density $C = \frac{\rho_0 R_g^3}{N} = 51.46$, where $R_g = \sqrt{N/6}$ is the BCP's unperturbed radius of gyration, and the NR volume fraction was held constant at $\phi_R = 0.5\%$. One of the goals of our work will be to explore the role of the surface selectivity towards the majority (B) block of the BCP, and the interactions with the wall were controlled by adding an additional term $S(\mathbf{r})$ to the chemical potential field experienced by the B segments, $w_B(\mathbf{r}) \rightarrow w_B(\mathbf{r}) + S(\mathbf{r})$, where

$$S(\mathbf{r}) = \lambda_w \hat{\rho}_{w,l}(\mathbf{r}). \tag{11}$$

Here, λ_w is the strength of the repulsion from the surface experienced by the B segments, and the subscript l on $\hat{\rho}_{w,l}$ indicates that the wetting is only applied to the lower surface in our simulation box; the top surface remains neutral. For all calculations presented below, A-wetting surfaces are modeled with $\lambda_w = 6$ and neutral surfaces use $\lambda_w = 0$. In all of our calculations, the thickness of the film between the surfaces was fixed at $5.3R_g$. Our simulation box dimensions were $10.1 \times 8.7 \times L_Z R_g$, and the number of collocation points used to resolve

our field theory was fixed at $M = 38 \times 36 \times 21$. Finally, in order to calculate the NR partition function, we employ a Gaussian quadrature where we discretize the integrals over the spherical angles θ and ϕ into N_u and $2N_u$ sites, respectively, with $N_u = 12$; we have previously shown that $N_u = 12$ is sufficient to achieve converged results in simulations using this model.[38]

3.5 Results and Discussion

A. P2VP–AuNRs in PS-b-P2VP Thin Films

The dispersion of P2VP-grafted AuNRs in films (63 nm) is studied as a function of AuNR volume fraction immediately after spin coating from the THF solution. Figure 3.1 shows TEM images of the P2VP–AuNRs (dark) in the PS-*b*-P2VP where the P2VP domains are circular (light) at volume fractions ranging from 1 to 0.25 vol%. At 1 vol%, large aggregates are observed with very few isolated AuNRs (Figure 3.1a). As the volume fraction is reduced to 0.8 vol%, aggregate size decreases but a majority of AuNRs remain in aggregates. As noted by the circles in Figure 3.1a and b, many of these aggregates consist of side-by-side bundles of AuNRs. This side-by-side arrangement was previously observed for identical P2VP-grafted AuNRs dispersed in P2VP homopolymer (5 kg mol^{-1}) films due to depletion attraction forces.[14] Figure 3.1c shows that as the AuNR volume percent decreases to 0.25, the AuNRs appear well dispersed as mainly individual AuNRs.

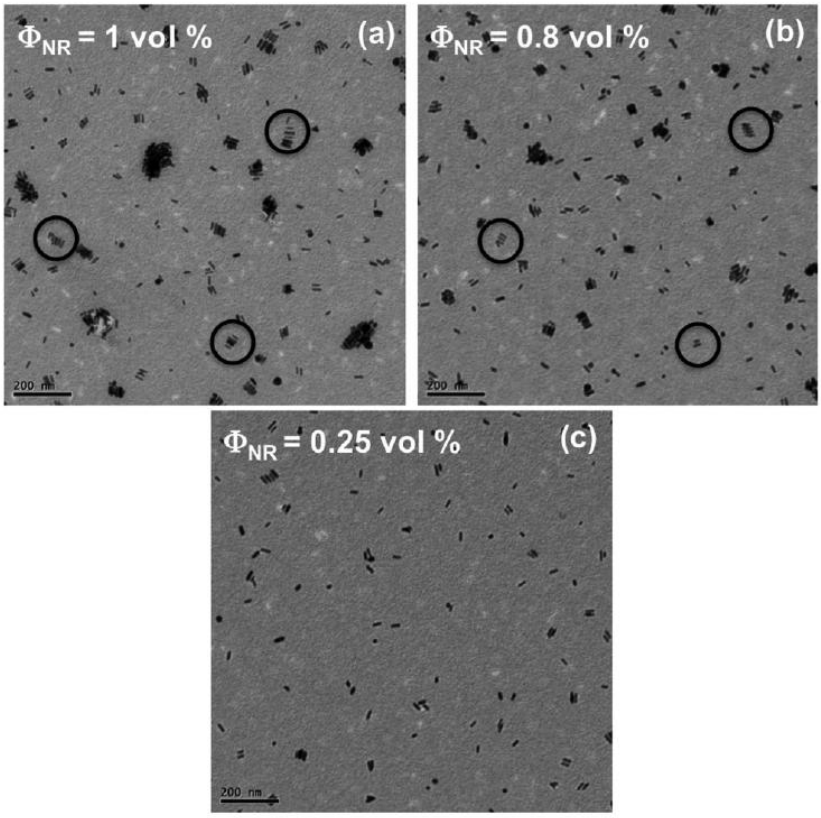

Figure 3.1. TEM images show the as-cast PS-*b*-P2VP films (63 nm) as a function of the volume percent of AuNRs (a) 1.0, (b) 0.80, and (c) 0.25. The circles denote the side by side arrangement of AuNRs in aggregates at 1 and 0.80 vol%. At 0.25 vol%, the AuNRs are well dispersed with a majority of individual AuNRs. The discrete white regions represent the P2VP minority domains in the as-cast film.

For PS–AuNR:PS and P2VP–AuNR:P2VP homopolymer matrices, aggregated and dispersed morphologies were distinguished by the fraction of isolated NRs viewed in TEM images.[14,15] For these homopolymer matrices, aggregation was defined as fewer than 50% individual nanorods. Using a similar approach, the fraction of isolated AuNRs at 1, 0.8 and 0.25 vol% are 12.4%, 18.7% and 67.5%, respectively. Although the criterion for AuNR

dispersion in homopolymer was set at 90%, most of the aggregates at 0.25 vol% consist of pairs of nanorods, and few large aggregates are observed. Therefore, for the P2VP–AuNR:PS-*b*-P2VP case, we consider the NRs to be dispersed in 63 nm films with 0.25 vol% AuNRs. The remainder of this paper will focus on P2VP–AuNR assembly at this concentration.

Figure 3.2 shows the AFM topography (left column) and phase (right column) images of P2VP–AuNR:PS-*b*-P2VP films after spin-coating from THF solution (a and b) and after solvent annealing in chloroform for one hour followed by UVO etching (c–j). THF is a good solvent for both the PS and P2VP blocks. Wang *et al.* spin-coated 300 nm thick films of PS-*b*-P2VP onto silicon from THF solution, where the PS-*b*-P2VP had P2VP as the minority block and the block copolymer was cylinder forming (volume fraction P2VP = 0.233),[56] and SEM of their as spin-coated film appears to show a mixture of parallel and perpendicular cylinders. This would suggest that the raised circular features in our AFM of the as-cast P2VP–AuNR:PS-*b*-P2VP are poorly ordered vertical cylinders, with some horizontal cylinders.

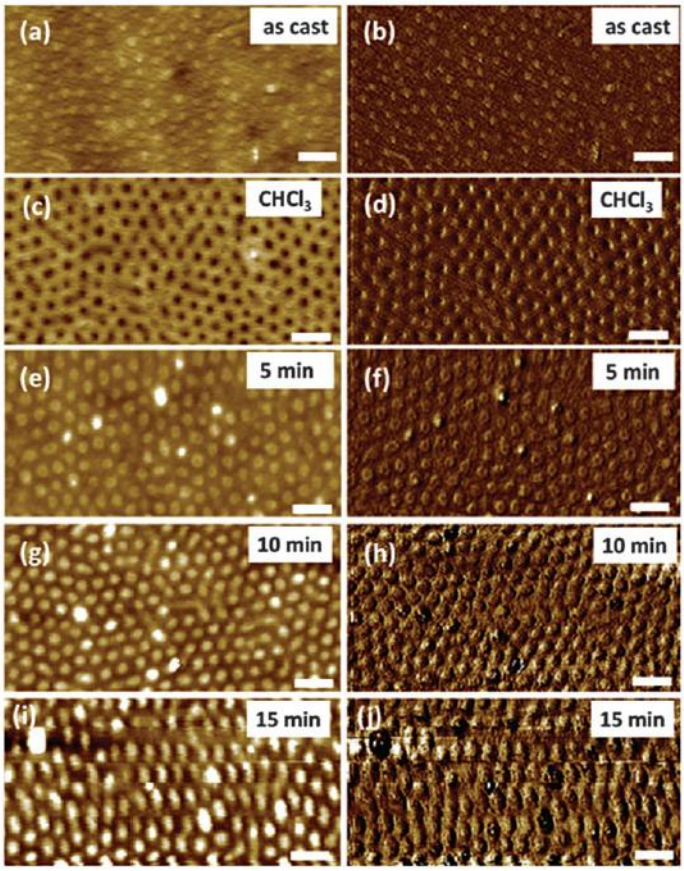

Figure 3.2. AFM topography (a, c, e, g, i) and phase images (b, d, f, h, j) of P2VP–AuNRs at 0.25 vol% in the PS-*b*-P2VP films. After spin coating from THF, the morphology of the dried film (63 nm) is shown in (a and b). The morphology after 1 hour solvent annealing and drying is shown in (c and d). This film is then exposed to UVO treatment for 5 min (e and f); 10 min (g and h); and 15 min (i and j). The average film thicknesses are 63, 63, 47, 32, and 17 nm, respectively. In the AFM images, the scale bar is 200 nm. The *Z*-scale is 15 nm and the phase scale is 10°.

The as-cast films were then solvent annealed in chloroform, which is a good solvent for both P2VP and PS blocks. As reviewed in a recent perspective,[57] solvent annealing can

lead to a rich variety of film morphologies independent of the bulk equilibrium morphology. It was recently demonstrated for PS-*b*-P2VP films as thick as 600 nm on silicon that solvent annealing in chloroform results in a vertical cylinder morphology.[58] Figure 3.2c and d show that a hexagonal-like array of circular features appears on the surface of the P2VP–AuNR:PS-*b*-P2VP film after solvent annealing suggesting the formation of a hexagonal vertical cylinder morphology. Based on the copolymer composition, the lower features in the topographic image (Figure 3.2c) are identified as the cylindrical P2VP minority phase, whereas the higher regions represent the majority PS matrix. The phase image in Figure 3.2d supports this interpretation. Line scans across topographic images (*e.g.*, Figure 3.2c) were performed to quantify the dimensions of the vertical cylinder morphology. The average height difference between the lower P2VP cylinders and higher PS matrix is 4.5 nm, whereas, the average center-to-center spacing between the vertical cylinders is 91 ± 7 nm. Cylinder forming PS(50 kg mol^{-1})-*b*-P2VP(16.5 kg mol^{-1}) films show a similar height difference of 2 nm.[58] Note that in both the as-cast (Figure 3.2a and b) and solvent annealed (Figure 3.2c and d) images, AuNRs are not observed on the surface or near the surface indicating that AuNRs are below the surface.

To reveal the location of the AuNRs, the P2VP–AuNR:PS-*b*-P2VP film solvent annealed in chloroform (*e.g.*, Figure 3.2c) was etched using UVO and then characterized by AFM. As shown in Figure 3.2e, after a 5 min exposure to UVO, the P2VP microdomains are higher (lighter) than the surrounding PS matrix (darker). Line scan analysis shows a height difference of 2.0 nm, whereas ellipsometry shows that the average thickness decreases from 63 to 47 nm. The inversion of height between the P2VP cylinders (*i.e.*, from low to high or dark to light in Figure 3.2c and e, respectively) and the PS matrix suggests the etching rate of

PS is faster than P2VP. Notably, after etching, higher (Figure 3.2e) circular regions emerge that coincide with the locations of the P2VP cylinders, suggesting that we are able to uncover the AuNRs with etching. After another 5 min UVO treatment on the same film (Figure 3.2g and h), the height difference between the higher P2VP domains and the PS matrix increases from 2.0 nm after 5 min to 4.5 nm after 10 min. The average film thickness after 10 min of etching is 32 nm which is approximately half the original film thickness and comparable to the length of the AuNRs. The P2VP domains remain circular and in a hexagonal array consistent with vertical cylinders. Similar to the 5 min etching case, high features that co-locate with the P2VP domains appear in the topography image (Figure 3.2g). Although statistics are limited, there appears to be an increasing number of rods closer to the substrate in the height image, although contrast in the phase image is not readily observed in Figure 3.2h. After another 5 min of UVO treatment (15 min total, Figure 3.2i and j), the film thickness decreases to 17 nm, which is less than the AuNR length of 28 nm. Moreover, the P2VP cylinders are now approximately 7.0 nm higher than the PS matrix. Although high regions are observed after 15 minutes of etching, the identification of the AuNRs is difficult because of the high surface roughness. In summary, AFM imaging combined with UVO etching suggests that NRs locate in the P2VP domains and locate preferentially near the substrate. Furthermore, AFM imaging indicates that the P2VP vertical cylinders extend from the surface to a depth of at least 46 nm (63–17 nm) below the surface.

To complement AFM imaging combined with UVO etching, TEM was used to provide top-down images of the P2VP–AuNR:PS-*b*-P2VP structure through the film thickness. Figure 3.3 shows TEM and AFM images for the P2VP–AuNR:PS-*b*-P2VP after solvent annealing (top) and after solvent annealing followed by 15 min UVO etching

(bottom). The images are plotted with the same scale bar of 200 nm for ease of comparison. Figure 3.3a shows light circular features of the P2VP domains in a hexagonal-like pattern. The AFM image in Figure 3.3b (bottom) and line scan (top) show that the P2VP domains are 4.5 nm below the PS matrix indicating that the contrast in Figure 3.3a results from a height difference. The AuNRs are reasonably well dispersed and, more importantly, more than 90% locate within the P2VP domains (white) in agreement with the observation from AFM/UVO etching experiments. A significant and somewhat surprising finding is that a majority of the AuNRs lay parallel to the substrate. Although a small percentage of AuNRs may indeed lie vertically within the vertical cylinders (red circles), further studies are needed to determine if these are indeed AuNRs or spherical impurities. As shown in Figure 3.3c, the TEM image after 15 min UVO exposure shows dark circular features (*i.e.*, the negative of Figure 3.3a). Figure 3.3d shows the AFM image (bottom) and line scan (top) where the P2VP domains are now higher (by ~7 nm) than the PS matrix. Therefore the darker domains also result from height contrast whereby the higher P2VP cylinders scatter electrons more strongly than the surrounding PS. As in Figure 3.3a, the AuNRs mainly lie parallel to the substrate. Although heat and radiation can cause the AuNRs to reshape,[59] the UVO treatment used in this study did not result in reshaping as supported by the fixed value of the aspect ratio, 3.6.

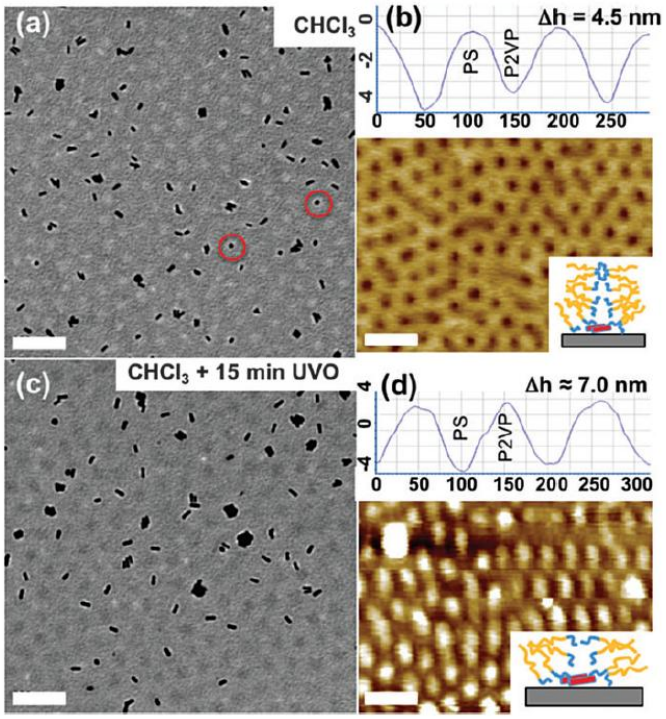

Figure 3.3. TEM and AFM topography images of P2VP–AuNRs(0.25 vol%):PS-*b*-P2VP films after solvent annealing (a and b) and after solvent annealing followed by 15 min of UVO treatment (c and d). The light circular regions in (a) correlate with the low P2VP domains in (b). Correspondingly, the dark circular regions in (c) correlate with the high P2VP domains in (d). Importantly, a majority of the AuNRs lie parallel to the substrate. A minority of AuNRs (red circles) may be vertically oriented. The scale bars are 200 nm.

On the basis of the previously described AFM and TEM analysis, we propose that the NRs preferentially locate at the base of the P2VP cylinders, which splay out to allow the P2VP block to wet the underlying substrate. This hypothesis is supported by the results from our CL simulations where A NRs are distributed in an A-cylinder forming AB diblock copolymer placed on an A-wetting substrate with a wetting parameter $\lambda_w = 6$, which causes

the minority block to preferentially wet the underlying substrate. Figure 3.4a shows the average density of the A block (blue) of the BCP as well as the regions that have a high concentration of the NRs (black) for vertical A cylinders against an A-wetting substrate. The thickness and lateral dimensions are normalized by the radius of gyration, R_g, of the diblock copolymer and approximately correspond to experimental values of the P2VP–AuNR:PS-*b*-P2VP system. The A domains become wider near the base in order to partially wet the underlying substrate. Although this captures the asymmetry of wetting of PS at the surface and P2VP at the substrate, it fails to capture the complete wetting of the P2VP block against the oxide. Vertically-oriented cylinders were unstable for substrate conditions that lead to a stronger asymmetry in the wetting. For the NR diameter and length in our system, CL simulations show that the NRs predominantly segregate to the base of the A cylinder.

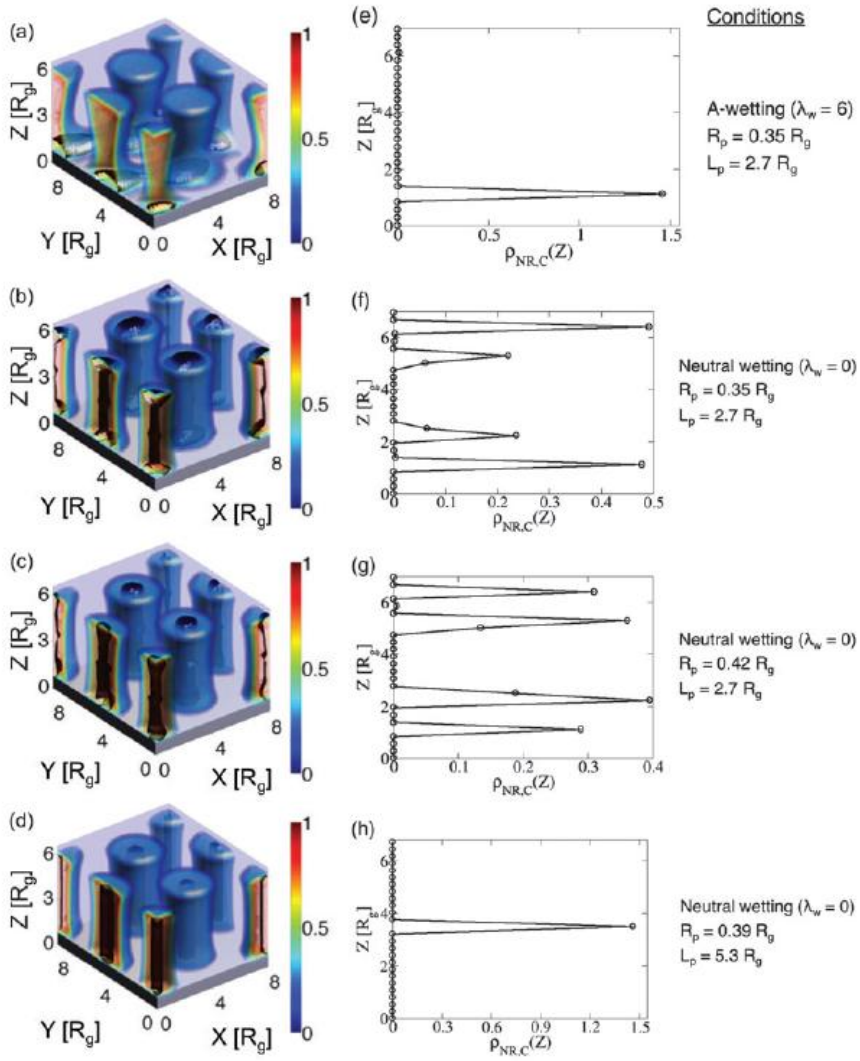

Figure 3.4. (a–d) Isosurface plots of the local density of the A-block of the diblock copolymer at various values of the wetting parameter λ_w and NR dimensions R_p and L_p. The *x*-, *y*-, and *z*-positions are normalized by the radius of gyration R_g of the simulated polymer. The color bars indicate the local volume fraction of the minority block of the diblock copolymer, while the black isosurfaces indicate regions with an average nanorod density greater than five times the average. (e)–(h) Distributions of the centers of mass of the NRs corresponding to the adjacent images. The NR center density $\rho_{NR,c}(z)$ is obtained

by integrating the nanorod density operator over all possible orientations and is defined in eqn (12).

We calculate the distribution of the NRs through the thickness of the film by integrating the density operator[38] over the plane of the film and all possible orientations of the nanorods,

$$\rho_{\mathrm{NR},c}(z) = \frac{n_{\mathrm{R}}}{4\pi V Q_{\mathrm{R}}} \int \mathrm{d}x \int \mathrm{d}y \int \mathrm{d}\mathbf{u} \mathrm{e}^{-w_{\mathrm{R}}(\mathbf{r},\mathbf{u})}. \tag{12}$$

Figure 3.4e shows the distribution of the nanorods' centers of mass as a function of depth in the film, and essentially all of the NRs locate near the A-wetting substrate. We calculate the fraction of the NRs with their center of mass beyond $2R_p$ of the surfaces and denote this as f_v, the number fraction of vertically oriented NRs. On the A-wetting substrates shown in Figure 3.4a, we find that essentially all of the NRs segregate to the base of the cylinders ($f_v = 0$). Both the experimental and simulation results showed that a majority of NRs locate near the base of the cylinders when the BCP is deposited on a surface that is preferentially wet by the minority component of the BCP.

In contrast, when the substrate is neutral towards both blocks ($\lambda_w = 0$), the NRs are much more likely to be found in a vertical orientation, (Figure 3.4b), and the fraction of vertical rods increases to $f_v = 41\%$. However, even though more NRs are driven into the cylinders, a significant fraction (59%) lies near and parallel to the top and bottom surfaces. Note that the NR distribution shown in Figure 3.4f reflects both the redistribution of NRs and their symmetry with respect to both interfaces. In addition to assisting with interpreting experimental studies, our CL model is a powerful tool for guiding future experiments; in

particular, the model can suggest experimental parameters that enhance the fraction of vertically oriented NRs by varying the dimensions of the rods. For example, if we fix the length of the NR while increasing the radius from $0.35R_g$ to $0.42R_g$, we find that the fraction of vertically oriented rods increases from 41% to 81%, as shown in Figure 3.4c and g. Alternatively, Figure 3.4d and h show that if NR radius has an intermediate value of $R_p = 0.39R_g$ while increasing the NR length from $L_p = 2.7R_g$ to $L_p = 5.3R_g$, nearly 100% of the NRs locate in the cylindrical domains and orient vertically with respect to the substrate.

Our hybrid particle/field theory simulation results shed light on the thermodynamic driving force behind the nanorod distribution. For each NR geometry and set of wetting conditions, we perform two calculations: one where a single, explicit nanorod is fixed at the base of the cylinder with its most probable orientation (which is horizontal, or in the plane of the film), and a second calculation where the explicit nanorod is fixed at its most probable position with a vertical orientation. For both nanorod positions and orientations, we calculate the average entropy per polymer chain[60] and denote the difference in the entropy of the diblocks between the vertical and horizontal orientations as $\Delta S_{vh} = S_v - S_h$, in units of k_B per chain. For the NRs with a radius of $R_p = 0.35R_g$ and $L_p = 2.7R_g$, $\Delta S_{vh} = -3.21 \times 10^{-2}$. The negative value indicates that the average entropy of the BCP chains is higher when the NR has a horizontal orientation, suggesting that the vertical orientation is entropically unfavorable. However, upon increasing the radius of the NR to $R_p = 0.42R_g$, ΔS_{vh} becomes positive and increases to 1.41×10^{-3}, indicating that the transition from horizontally aligned NRs to vertical NRs is at least partially driven by the entropy gained by the polymer chains. We note that the magnitudes of the values are relatively small because the calculation

averages over all of the chains in our system, including chains far away from the NR, and that this neglects any entropic contributions from many-body nanorod interactions. A more thorough exploration of the simulation system parameters will be published in a forthcoming manuscript.

3.6 Conclusions

In this paper, we have investigated the dispersion and alignment of P2VP–AuNRs in cylinder-forming PS-*b*-P2VP in 63 nm films. Upon chloroform solvent annealing of P2VP–AuNR:PS-*b*-P2VP films, a hexagonally ordered vertical P2VP-cylinder morphology is obtained where the P2VP domains are lower than the surrounding matrix. To detect the AuNRs and follow the P2VP morphology through the film thickness, sequential UVO etching is combined with AFM. In both topography and phase imaging, features appear after etching that co-locate with the P2VP domains that are suggestive of the AuNRs. Because P2VP etch rate is slower than that of PS, a height inversion is observed where the P2VP domains become higher than the PS matrix. As etching time increases the height difference also increases as well as the number of features suggestive of AuNRs. By taking advantage of the height difference between the P2VP and PS domains, no iodine staining is required to distinguish between the domains in TEM imaging of the solvent annealed or solvent annealed and UVO etched samples. A majority of the AuNRs locate near the substrate in the vicinity where the P2VP domain transitions from vertical to wetting the substrate. Experimental observations are supported by complex Langevin field theoretic simulations using material parameters that capture the experimental system, namely length and radius of the AuNR, film thickness, and polymer/interface wetting. Our simulations suggest that both

the substrate wetting and the nanorod geometry relative to the size of the polymer dictates whether the NRs adopt a vertical orientation, and some of the driving force for the NRs to adopt a vertical orientation comes from the entropy of the diblock polymers. The CL simulations indicate the AuNRs locate near the substrate to relieve chain stretching of the P2VP block near the junction. In addition to assisting with interpreting our experiments, our simulation studies propose system parameters to guide future studies aimed at controlling the alignment of NRs by changing either the nanorod geometry or the wetting properties of the substrate.

3.7 References

1. M. Grzelczak, J. Perez-Juste, P. Mulvaney and L. M. Liz-Marzan, *Chem. Soc. Rev.*, 2008, **37**, 1783.
2. C. B. Murray, D. J. Norris and M. G. Bawendi, *J. Am. Chem. Soc.*, 1993, **115**, 8706.
3. C.-C. Chen, C.-Y. Chao and Z.-H. Lang, *Chem. Mater.*, 2000, **12**, 1516.
4. L. Carbone, C. Nobile, M. De Giorgi, F. D. Sala, G. Morello, P. Pompa, M. Hytch, E. Snoeck, A. Fiore, I. R. Franchini, M. Nadasan, A. F. Silvestre, L. Chiodo, S. Kudera, R. Cingolani, R. Krahne and L. Manna, *Nano Lett.*, 2007, **7**, 2942.
5. M. Rycenga, C. M. Cobley, J. Zeng, W. Li, C. H. Moran, Q. Zhang, D. Qin and Y. Xia, *Chem. Rev.*, 2011, **111**, 3669.
6. R. B. Thompson, V. V. Ginzburg, M. W. Matsen and A. C. Balazs, *Science*, 2001, **292**, 2469.
7. A. C. Balazs, T. Emrick and T. P. Russell, *Science*, 2006, **314**, 1107.

8. M. R. Bockstaller, Y. Lapetnikov, S. Margel and E. L. Thomas, *J. Am. Chem. Soc.*, 2003, **125**, 5276.
9. J. J. Chiu, B. J. Kim, E. J. Kramer and D. J. Pine, *J. Am. Chem. Soc.*, 2005, **127**, 5036.
10. Y. Lin, A. Böker, J. He, K. Sill, H. Xiang, C. Abetz, X. Li, J. Wang, T. Emrick, S. Long, Q. Wang, A. Balazs and T. P. Russell, *Nature*, 2005, **434**, 55.
11. M. R. Bockstaller, R. A. Mickiewicz and E. L. Thomas, *Adv. Mater.*, 2005, **17**, 1331.
12. M. J. A. Hore and R. J. Composto, *ACS Nano*, 2010, **4**, 6941.
13. A. L. Frischknecht, M. J. Hore, J. Ford and R. J. Composto, *Macromolecules*, 2013, **46**, 2856.
14. G. Jiang, M. J. A. Hore, S. Gam and R. J. Composto, *ACS Nano*, 2012, **6**, 1578.
15. M. J. A. Hore, A. L. Frischknecht and R. J. Composto, *ACS Macro Lett.*, 2012, **1**, 115.
16. M. J. A. Hore and R. J. Composto, *Macromolecules*, 2014, **47**, 875.
17. K. Thorkelsson, J. H. Nelson, A. P. Alivisatos and T. Xu, *Nano Lett.*, 2013, **13**, 4908.
18. J. Kao, K. Thorkelsson, P. Bai, B. J. Rancatore and T. Xu, *Chem. Soc. Rev.*, 2013, **42**, 2654.
19. E. Ploshnik, A. Salant, U. Banin and R. Shenhar, *Adv. Mater.*, 2010, **22**, 2774.
20. J. G. Son, W. K. Bae, H. Kang, P. F. Nealey and K. Char, *ACS Nano*, 2009, **3**, 3927.
21. Z. Liu, H. Huang and T. He, *Small*, 2013, **9**, 505.
22. R. D. Deshmukh, Y. Liu and R. J. Composto, *Nano Lett.*, 2007, **7**, 3662.
23. C.-T. Lo, M.-H. Li and W.-T. Lin, *J. Chem. Phys.*, 2015, **142**, 184903.

24. A. Halevi, S. Halivni, M. Oded, A. H. Muller, U. Banin and R. Shenhar, *Macromolecules*, 2014, **47**, 3022.
25. K. Thorkelsson, A. J. Mastroianni, P. Ercius and T. Xu, *Nano Lett.*, 2012, **12**, 498.
26. E. Ploshnik, A. Salant, U. Banin and R. Shenhar, *Phys. Chem. Chem. Phys.*, 2010, **12**, 11885.
27. Q. Zhang, S. Gupta, T. Emrick and T. P. Russell, *J. Am. Chem. Soc.*, 2006, **128**, 3898.
28. C.-T. Lo and W.-T. Lin, *J. Phys. Chem. B*, 2013, **117**, 5261.
29. W. Li, P. Zhang, M. Dai, J. He, T. Babu, Y.-L. Xu, R. Deng, R. Liang, M.-H. Lu and Z. Nie, *et al.* , *Macromolecules*, 2013, **46**, 2241.
30. C. A. Breen, T. Deng, T. Breiner, E. L. Thomas and T. M. Swager, *J. Am. Chem. Soc.*, 2003, **125**, 9942.
31. J. Listak and M. R. Bockstaller, *Macromolecules*, 2006, **39**, 5820.
32. G. N. Toepperwein and J. J. De Pablo, *Macromolecules*, 2011, **44**, 5498.
33. G. N. Toepperwein, N. C. Karayiannis, R. A. Riggleman, M. Kröger and J. J. De Pablo, *Macromolecules*, 2011, **44**, 1034.
34. G. N. Toepperwein, K. S. Schweizer, R. A. Riggleman and J. J. De Pablo, *Macromolecules*, 2012, **45**, 8467.
35. Z. Shou, G. A. Buxton and A. C. Balazs, *Compos. Interfaces*, 2003, **10**, 343.
36. Q.-Y. Tang and Y.-Q. Ma, *J. Phys. Chem. B*, 2009, **113**, 10117.
37. J. Koski, H. Chao and R. A. Riggleman, *J. Chem. Phys.*, 2013, **139**, 244911.
38. H. Chao, B. A. Hagberg and R. A. Riggleman, *Soft Matter*, 2014, **10**, 8083.
39. J. Koski, H. Chao and R. A. Riggleman, *Chem. Commun.*, 2015, **51**, 5440.

40. S. Sides, B. Kim, E. Kramer and G. Fredrickson, *Phys. Rev. Lett.*, 2006, **96**, 250601.
41. T. K. Sau and C. J. Murphy, *Langmuir*, 2004, **20**, 6414.
42. B. Nikoobakht and M. A. El-Sayed, *Chem. Mater.*, 2003, **15**, 1957.
43. W. S. Rasband, "ImageJ," http://imagej.nih.gov/ij, 1997–2014.
44. S. K. Kumar, N. Jouault, B. Benicewicz and T. Neely, *Macromolecules*, 2013, **46**, 3199.
45. P. F. Green, *Soft Matter*, 2011, **7**, 7914.
46. S. Srivastava, P. Agarwal and L. A. Archer, *Langmuir*, 2012, **28**, 6276.
47. T. B. Martin, K. I. S. Mongcopa, R. Ashkar, P. Butler, R. Krishnamoorti and A. Jayaraman, *J. Am. Chem. Soc.*, 2015, **137**, 10624.
48. E. Helfand, *J. Chem. Phys.*, 1975, **62**, 999.
49. M. W. Matsen, *J. Chem. Phys.*, 1997, **106**, 7781.
50. Z.-G. Wang, *Phys. Rev. E: Stat., Nonlinear, Soft Matter Phys.*, 2010, **81**, 21501.
51. R. A. Riggleman, R. Kumar and G. H. Fredrickson, *J. Chem. Phys.*, 2012, **136**, 24903.
52. M. C. Villet and G. H. Fredrickson, *J. Chem. Phys.*, 2014, **141**, 224115.
53. G. H. Fredrickson, *The Equilibrium Theory of Inhomogeneous Polymers*, Oxford University Press, New York, 2006.
54. G. H. Fredrickson, V. Ganesan and F. Drolet, *Macromolecules*, 2002, **35**, 16.
55. E. M. Lennon, G. O. Mohler, H. D. Ceniceros, C. J. García-Cervera and G. H. Fredrickson, *Multiscale Model. Simul.*, 2008, **6**, 1347.
56. Y. Wang, C. He, W. Xing, F. Li, L. Tong, Z. Chen, X. Liao and M. Steinhart, *Adv. Mater.*, 2010, **22**, 2068.

57. C. Sinturel, M. Vayer, M. Morris and M. A. Hillmyer, *Macromolecules*, 2013, **46**, 5399.

58. J. Yin, X. Yao, J.-Y. Liou, W. Sun, Y.-S. Sun and Y. Wang, *ACS Nano*, 2013, **7**, 9961.

59. Y. Liu, E. N. Mills and R. J. Composto, *J. Mater. Chem.*, 2009, **19**, 2704.

60. M. W. Matsen, *J. Phys.: Condens. Matter*, 2001, **14**, R21.

CHAPTER 4: Nanorod Position and Orientation in Vertical Cylinder Block Copolymer Films

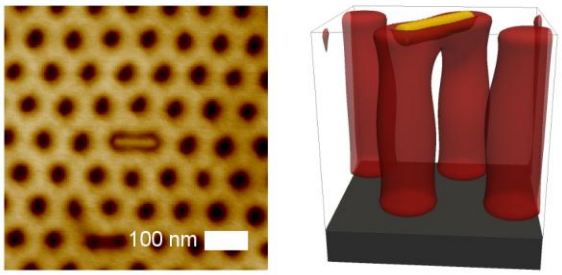

This chapter has been submitted for publication with the following authors: Boris Rasin, Benjamin J. Lindsay, Xingchen Ye, Jeffrey S. Meth, Christopher B. Murray, Robert A. Riggleman, and Russell J. Composto

4.1 Abstract

The self-assembly of gold nanorods (AuNRs) of different sizes with a block copolymer (BCP) is studied. Polystyrene-*block*-poly(2-vinylpyridine) (PS-*b*-P2VP) films containing P2VP functionalized AuNRs are solvent annealed resulting in a BCP morphology of vertical P2VP cylinders in a PS matrix. At the surface of the PS-*b*-P2VP films long AuNRs are found in the bridging and vertical states. The bridging state is where the long axis of the AuNR is parallel to the film surface, the AuNR is embedded in the film, and each end of the AuNR is at the top of nearest neighbor P2VP cylinders. The vertical state is where the AuNR is localized within a vertical P2VP cylinder, the AuNR long axis is perpendicular to the film surface and the upper tip of the AuNR is at the film

surface. Short AuNRs were found in the bridging and vertical states as well as in a state not observed for the long AuNRs, the centered state. The centered state is where an AuNR has its long axis parallel to the film surface, is embedded in the film, and is centered over a vertical P2VP cylinder. Hybrid particle-field theory (HPFT) simulations modeling the experimental system predict that for the long AuNRs only the bridging state should be observed while for the short AuNRs only the bridging and centered states should be observed. Possible explanations for why the vertical state is observed in experiments despite being thermodynamically unfavorable in simulations are discussed. HPFT simulations also show that when a nanorod is in the bridging state the two cylinders it bridges remain intact and extend from the nanorod to the substrate. Further, the minority block of the BCP is shown to wet the bottom of the bridging nanorod. The bridging state is very promising for the future development of self-assembled nanoscale devices.

4.2 Introduction

Nanoparticle-block copolymer (NP-BCP) self-assembly is a powerful approach for controlling NP position and orientation in polymer nanocomposites (PNCs). Control of NP position and orientation in PNCs allows the fabrication of PNC devices and the engineering of PNC properties. For example, metal NPs could be positioned in PNCs to form chains of non-touching metal NPs, resulting in metal NP plasmon waveguides.[1] Thus, it is important to continue to improve our understanding of and to continue to develop NP-BCP self-assembly.

NP-BCP self-assembly is typically implemented by solvent annealing or thermal annealing a PNC consisting of NPs and a BCP. The BCP self-assembles into a periodic morphology; for example a linear diblock copolymer can self-assemble into a hexagonal lattice of cylinders formed from one block in a matrix of the other block.[2] The NPs assume specific positions and orientations in the BCP morphology.[3] For example, NPs can be localized in the microdomains formed by one of the blocks or be located at the interfaces between microdomains.[4]

Spherical NP-BCP self-assembly has been extensively studied.[4-11] By comparison, studies of nanorod-BCP self-assembly are an emerging area of research.[12-22] In this work we study the position and orientation of nanorods in vertical cylinder BCP films. Nanocomposite films of polystyrene-*block*-poly(2-vinylpyridine) (PS-*b*-P2VP) and P2VP functionalized gold nanorods (AuNRs) were solvent annealed resulting in the PS-*b*-P2VP assuming a morphology of vertical P2VP cylinders in a PS matrix. At the surface of films prepared with long AuNRs, AuNRs were in the bridging and vertical states. The bridging state is where the long axis of the AuNR is parallel to the film surface, the AuNR is embedded in the film, and each end of the AuNR is at the top of nearest neighbor vertical cylinders. The vertical state is where the long axis of the AuNR is perpendicular to the film surface, the AuNR is localized in a vertical cylinder, and the upper tip of the AuNR is at the film surface. At the surface of films prepared with shorter AuNRs, AuNRs were found in the bridging, vertical, and centered states. The centered state is where the long axis of the AuNR is parallel to the film surface, the AuNR is embedded in the film and the AuNR is located on top of one vertical P2VP cylinder.

The free energy of the bridging, centered and vertical states as a function of nanorod length was calculated with hybrid particle-field theory (HPFT) simulations. At the surface of films containing the long AuNRs, the simulations predicted that only the bridging state should be observed, whereas both the bridging and centered states were predicted for shorter AuNRs. The simulations also predicted that the vertical state should not be observed. HPFT simulations were also used to study the BCP morphology when a nanorod is in the bridging state. The simulations showed that when an AuNR is in the bridging state, the bridged vertical cylinders remain intact and there is a minority block wetting layer underneath the AuNR.

4.3 Results and Discussion

Neat PS-*b*-P2VP Films with a Vertical Cylinder Morphology

Neat PS-*b*-P2VP films with a morphology of vertical P2VP cylinders in a PS matrix were prepared *via* solvent annealing. The films were prepared following the method of Yin *et al*.[23] A diblock copolymer of PS(M_n = 180,000 g mol^{-1})-*b*-P2VP(M_n = 77,000 g mol^{-1}) was spin-coated from chloroform on silicon wafers. The PS-*b*-P2VP films had a thickness of 363 nm. Atomic force microscopy (AFM) topography images of the as-spin-coated PS-*b*-P2VP films show a mixture of trenches and circular pits (Figure A.1). To obtain a vertical cylinder morphology the films were solvent annealed in chloroform. During solvent annealing the PS-*b*-P2VP film absorbs chloroform and swells. The chloroform in the film reduces the BCP glass transition temperature which increases the mobility of the BCP chains and allows the film structure to change.[24-26]

To determine the optimum solvent annealing time that produces a vertical cylinder morphology, films were solvent annealed from 7:30 (min:s) to 17:30. AFM topography images of the surfaces after solvent annealing show that films annealed between 13:45 and 16:15 have a surface topography of circular depressions forming a hexagonal lattice (Figure A.2).

Films solvent annealed for 14:23 were further analyzed and later selected for the polymer nanocomposite studies. AFM topography images of PS-*b*-P2VP films solvent annealed for 14:23 show a hexagonal lattice of circular depressions as seen in Figure 4.1a. Figure 4.1b shows a line profile passing through the centers of the depressions in a row of nearest neighbor depressions. The minima in the line profile correspond to the bottoms of the depressions. The average depth of the depressions was 11.5 nm.

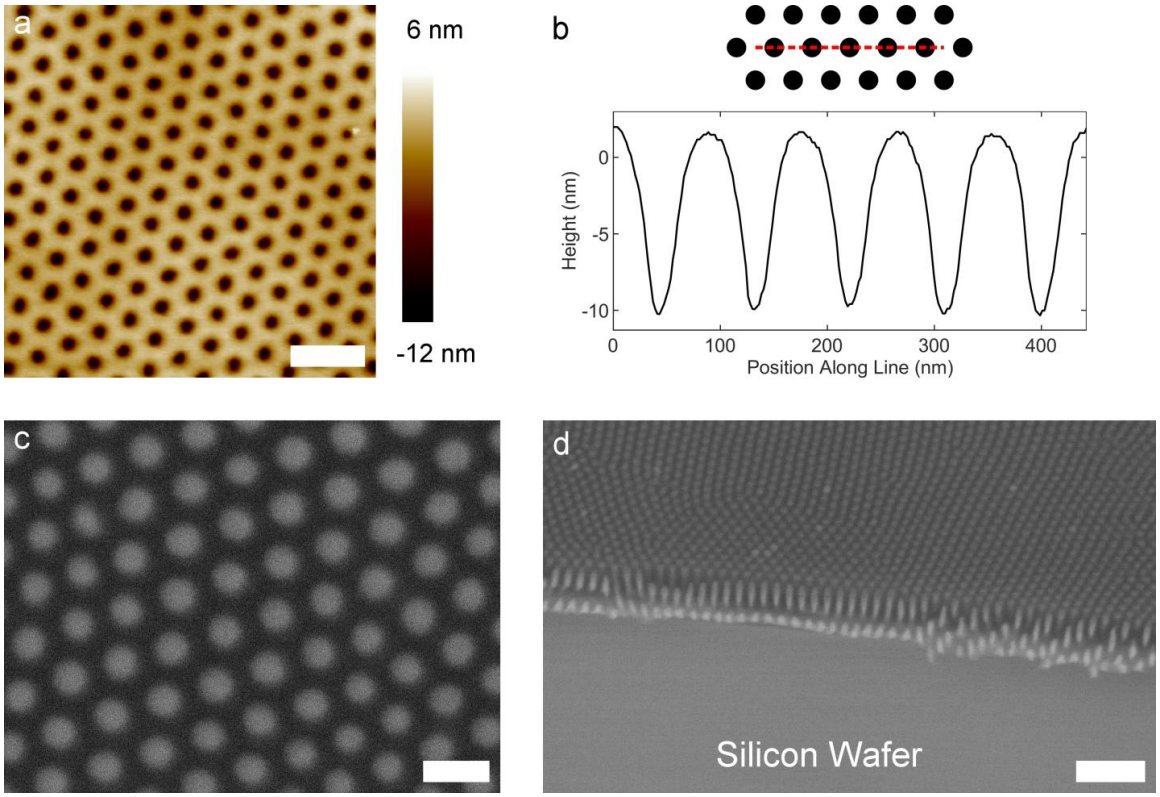

Figure 4.1. Characterization of neat vertical cylinder PS-*b*-P2VP films prepared by solvent annealing for 14:23. (a) AFM topography image. The lower (dark) circular regions are the tops of P2VP cylinders. The scale bar is 200 nm. (b) Line profile from the AFM image in (a) with the path of the line profile (dashed red line) relative to the tops of the P2VP cylinders shown in a schematic. (c) Top-down SEM image. The film was stained with iodine vapor causing the P2VP domains to appear brighter in the SEM image. The scale bar is 100 nm. (d) SEM image of a film cross-section. This film was also stained with iodine vapor prior to imaging. The scale bar is 500 nm.

To complement AFM studies, scanning electron microscopy (SEM) was used to characterize films solvent annealed for 14:23. Films were exposed to iodine vapor which selectively stains P2VP domains which appear brighter than PS domains in SEM. Figure 4.1c, a top-down SEM image of a PS-*b*-P2VP film, shows circular features (light) forming a hexagonal lattice surrounded by a continuous region (dark). The silicon substrates supporting the films were cleaved to expose the film cross-section. Figure 4.1d shows an SEM image of a film cross-section. Light stripes perpendicular to the film surface extend from the surface nearly to the bottom of the film. These stripes are regularly spaced and separated by darker regions. The white lines do not extend all the way to the substrate because the interface generated from the cleaving process is not the ideal flat vertical interface. The surface of the film, visible in the top half of Figure 4.1d, is consistent with top-down SEM (Figure 4.1c) with brighter circles forming a hexagonal lattice surrounded by a dark background.

From the top-down and cross-section SEM images we conclude that the morphology of the PS-*b*-P2VP films solvent annealed for 14:23 is vertical P2VP cylinders in a PS matrix with the vertical P2VP cylinders extending from the substrate to the film surface. In the top-down view the light circular features forming a hexagonal lattice are P2VP cylinders being viewed along their axis which is perpendicular to the film surface and the dark surrounding background is the PS matrix. The light stripes in the SEM cross-section are the vertical P2VP cylinders being viewed from the side. From the top-down SEM images we determined the P2VP cylinder diameter to be 43 nm. The center-to-center spacing between a cylinder and a nearest neighbor cylinder was 83 nm.

With the morphology of the film elucidated from SEM, it is clear that the hexagonally arranged depressions observed in AFM topography images are the tops of vertical P2VP cylinders and the higher surrounding region is the PS matrix. Our hypothesis for why the tops of the P2VP cylinders are 11.5 nm deep depressions is as follows. Elbs and Krausch showed that when exposed to chloroform vapor P2VP films increase in thickness more than PS films.[27] Consequently, when our PS-*b*-P2VP films are solvent annealed in chloroform the volume fraction of chloroform in the P2VP domains is greater than the volume fraction of chloroform in the PS domains. As a result when the chloroform evaporates the volume of the P2VP domains decreases more than the volume of the PS domains resulting in the formation of basins at the top of the P2VP cylinders. All nanocomposite films described in this study were solvent annealed for 14:23.

Position and Orientation of AuNRs in PS-*b*-P2VP Films with a Vertical Cylinder Morphology

The position and orientation of AuNRs functionalized with P2VP in vertical cylinder PS-*b*-P2VP films was studied. Nanocomposite films consisting of PS-*b*-P2VP and AuNRs were prepared by spin-coating a solution of PS-*b*-P2VP and AuNRs grafted with thiol-terminated P2VP(M_n = 2500 g mol^{-1}) in chloroform on silicon wafers. Nanocomposite films were prepared with AuNRs of two different sizes. One set of nanocomposites was prepared with AuNRs with a length of 101 nm and a diameter of 16 nm. The other set of nanocomposites was prepared with AuNRs with a length of 70 nm and a diameter of 12 nm. Both sets of nanocomposites had an AuNR weight fraction of 0.01 which corresponds to an AuNR volume fraction of 5.6×10^{-4}. After spin-coating, the

nanocomposite films were solvent annealed in chloroform for 14:23. We will denote the solvent annealed PS-*b*-P2VP-(101 nm length by 16 nm diameter AuNR) nanocomposites as PS-*b*-P2VP-AuNR101 and the solvent annealed PS-*b*-P2VP-(70 nm length by 12 nm diameter AuNR) nanocomposites as PS-*b*-P2VP-AuNR70.

Position and Orientation of AuNRs in PS-*b*-P2VP-AuNR101 Films

AFM characterization was performed on PS-*b*-P2VP-AuNR101 films. As shown in Figure 4.2a, the topography images of the surface show a similar structure as the neat films (Figure 4.1a), namely a hexagonal lattice of circular depressions. This result suggests that PS-*b*-P2VP-AuNR101 films have a morphology of vertical P2VP cylinders in a PS matrix with the depressions at the surface corresponding to the tops of vertical P2VP cylinders and the surrounding higher region corresponding to the PS matrix. We found that the circular depressions on the surface had a depth of 7.8 nm which is shallower than the value for the neat films, 11.5 nm. AuNRs are observed at the surface of PS-*b*-P2VP-AuNR101 films in the AFM topography images (Figure 4.2a,b). We found that 95% of AuNRs at the surface were in the "bridging state" shown in Figure 4.2b. The bridging state is where the AuNR is embedded in the film, the AuNR long axis is parallel to the film surface and one end of the AuNR is at the top of a given P2VP cylinder while the other end is at the top of a P2VP cylinder that is a nearest neighbor of the given P2VP cylinder. We found that 63% of AuNRs in the bridging state were not at a defect in the hexagonal lattice. Our definition for an AuNR not at a defect in the hexagonal lattice is given in the Methods. Figure 4.2b shows an AFM image of an AuNR in the bridging state not at a defect in the hexagonal lattice, whereas Figure 4.3 shows an AFM image of an

AuNR in the bridging state at a defect in the hexagonal lattice. The 5% of AuNRs at the surface not in the bridging state were embedded in the film and their long axis was parallel to the film surface. However, the lattice around these AuNRs was so defective that we could not determine whether the AuNRs were bridging vertical cylinders or in a different state.

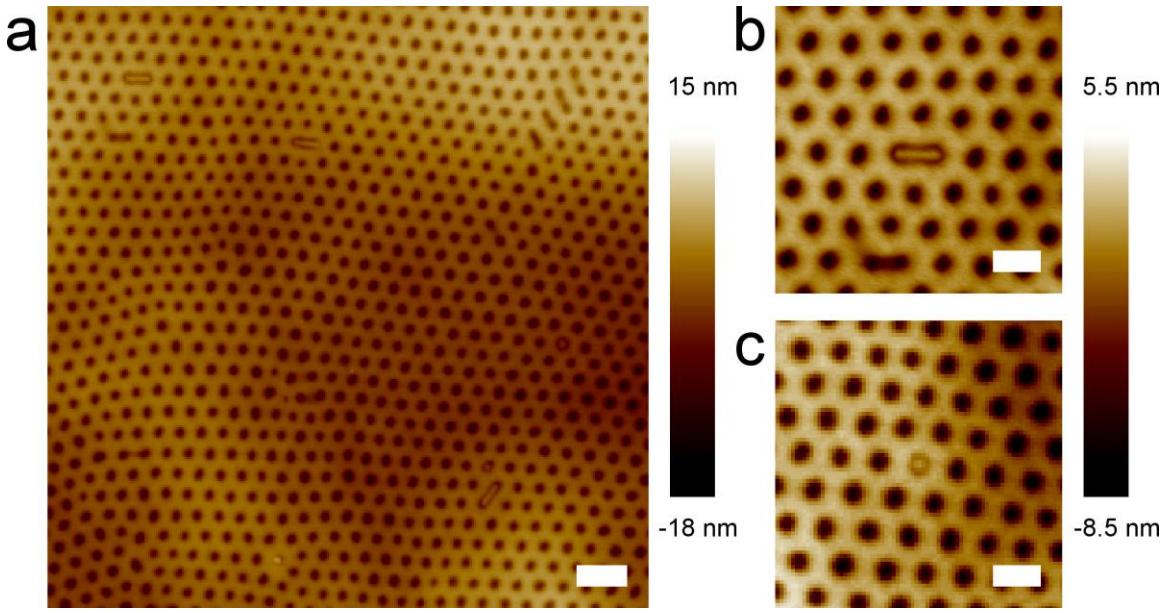

Figure 4.2. AFM topography images of the surface of PS-*b*-P2VP-AuNR101 films. (a) Large area AFM image showing three AuNRs in the bridging state. A circular feature can also be observed at the top of some vertical cylinders. The scale bar is 200 nm. (b) AFM image of an AuNR in the bridging state not at a defect in the vertical cylinder lattice. The AuNR is the same AuNR as that in the top left corner of image (a). The scale bar is 100 nm. (c) AFM image of a circular feature colocalized with a vertical P2VP cylinder. The scale bar is 100 nm.

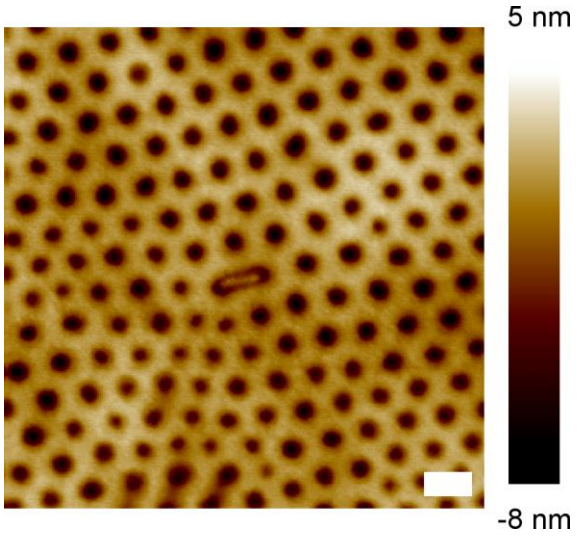

Figure 4.3. AFM topography image of an AuNR in the bridging state at a defect in the vertical cylinder lattice. The scale bar is 100 nm.

The position and orientation of bridging AuNRs that are not at a defect in the hexagonal lattice is analyzed in greater detail. From AFM images (*e.g.*, Figure 4.2b), the top of the AuNRs, defined as the midpoint of the line defined by the crest of the AuNR, was on average 1.6 nm below the PS matrix. Figure 4.4 is a line profile along the crest of a bridging AuNR not at a defect in the lattice which shows the relative heights of the top of the AuNR (center of image) and the PS matrix (continuous phase). Further we observed that the region immediately surrounding the AuNRs was 2.0 nm lower than the top of the AuNRs. The AuNRs were almost completely parallel to the surface with an average angle between the long axis of the AuNR and the surface of 0.9°. This can be seen in the line profile in Figure 4.4. Like the bridging AuNRs not at a defect in the hexagonal lattice the bridging AuNRs at defects in the hexagonal lattice were almost

completely parallel to the surface. However, the top of these AuNRs varied from 1 nm above the PS matrix to below the PS matrix.

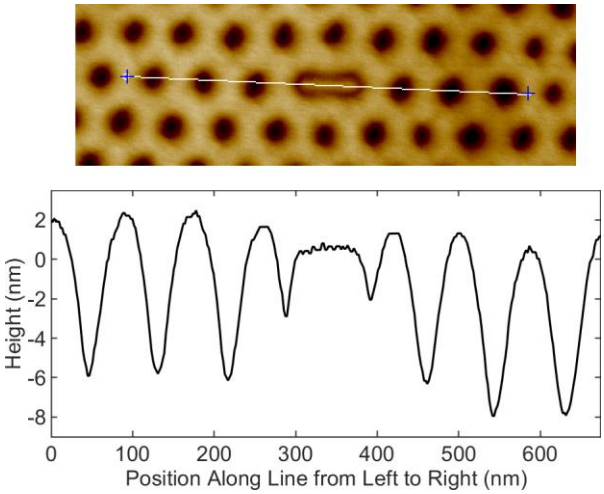

Figure 4.4. Line profile from the AFM image in Figure 4.2b along the crest of the AuNR in the bridging state not at a defect in the vertical cylinder lattice. The path of the line profile is shown via a line on the AFM image at the top of the figure.

The AFM topography images of the surface of the PS-*b*-P2VP-AuNR101 films also show that some vertical cylinders have a circular feature at their top as shown in Figure 4.2c. One explanation is that the circular feature corresponds to a vertically oriented AuNR localized within a P2VP cylinder and positioned with its upper tip at the film surface. A second explanation is that a circular feature is a gold nanosphere localized within a P2VP cylinder and positioned at the film surface. Gold nanospheres are present in the PS-*b*-P2VP-AuNR101 films as they are a very minor product in AuNR synthesis.

Top-down SEM images of the PS-*b*-P2VP-AuNR101 films show that there are AuNRs at the surface of the films and that the AuNRs are parallel to the surface of the

films (Figure 4.5). These observations are consistent with AFM studies shown in Figure 4.2. Nanoparticles below the surface of a film appear blurry while those at the surface of a film are sharp allowing us to determine whether a nanoparticle is at or below the surface of a film. Circular features are also observed at the surface of the films matching our observation of circular features colocalized with vertical P2VP cylinders in AFM images. The SEM images show AuNRs that are not vertically oriented below the surface of the films. This shows that there are AuNRs below the surface of the films that are not localized within vertically oriented P2VP cylinders. Circular features are also observed below the surface of the films. These features could be vertically oriented AuNRs or gold nanospheres.

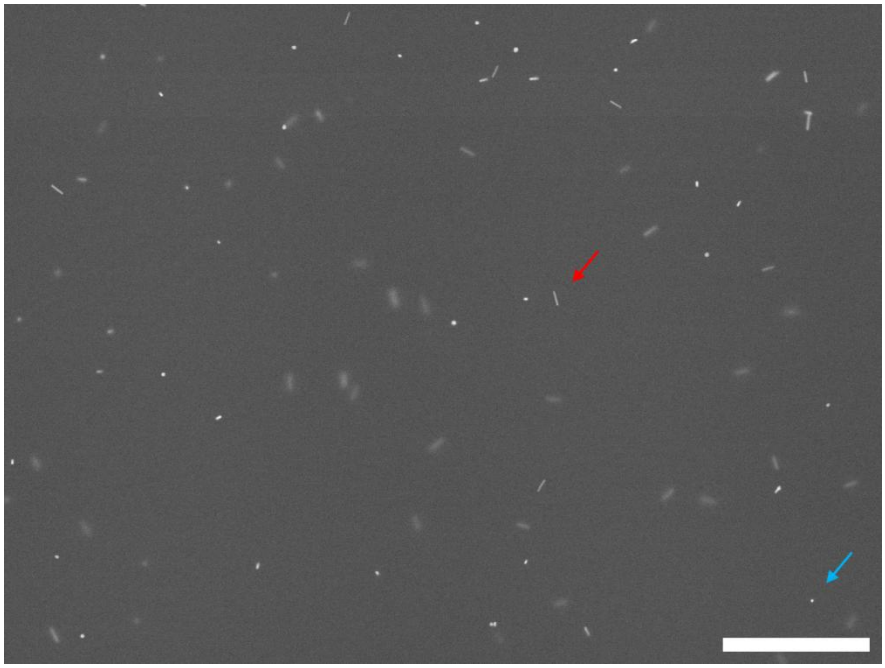

Figure 4.5. Top-down SEM image of a PS-*b*-P2VP-AuNR101 film. The red arrow points to a nanorod at the film surface that is parallel to the film surface. The blue arrow points to a circular feature at the film surface. The scale bar is 1 µm.

We also examined the cross-sections of the PS-*b*-P2VP-AuNR101 films with SEM (Figure 4.6). The SEM images show that at the surface of the films there are vertical AuNRs with their tip at the surface of the film (blue arrows in Figure 4.6). The SEM images also show AuNRs parallel to the surface of the films at the surface of the films and circular features at the surface of the films. Our observation of a circular feature at the top of some vertical cylinders in AFM suggests that the vertical AuNRs at the surface of the film are localized within a vertical P2VP cylinder. The observation of AuNRs parallel to the film surface at the film surface matches our AFM and top-down SEM results. Circular features observed at the film surface could be either gold

nanospheres or AuNRs being viewed end-on. AuNRs are also observed in the films. AuNRs in the films have many different orientations showing that AuNRs in the films are not localized within vertical P2VP cylinders. Circular features are observed in the films which could be either gold nanospheres or AuNRs being viewed end-on.

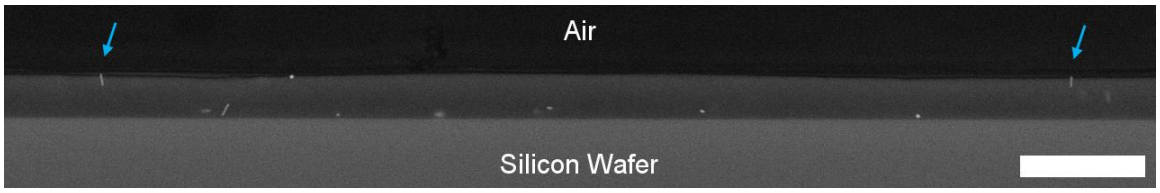

Figure 4.6. SEM image of the cross-section of a PS-*b*-P2VP-AuNR101 film. The blue arrows point to vertically oriented AuNRs with their tip at the surface of the film. The scale bar is 1 μm.

Position and Orientation of AuNRs in PS-*b*-P2VP-AuNR70 Films

The surfaces of PS-*b*-P2VP-AuNR70 nanocomposite films were characterized with AFM. As shown in Figure 4.7a, AFM topography images of the film surface show the same hexagonal lattice of circular depressions observed in the AFM topography images of the neat films (Figure 4.1a). This result suggests that the nanocomposite films have a morphology of vertical P2VP cylinders in a PS matrix. The depressions are the tops of vertical P2VP cylinders and the surrounding region is the PS matrix. The depth of the circular depressions at the surface of the PS-*b*-P2VP-AuNR70 nanocomposite films was 9.6 nm which was less than the depth of the circular depressions at the surface of neat vertical cylinder films.

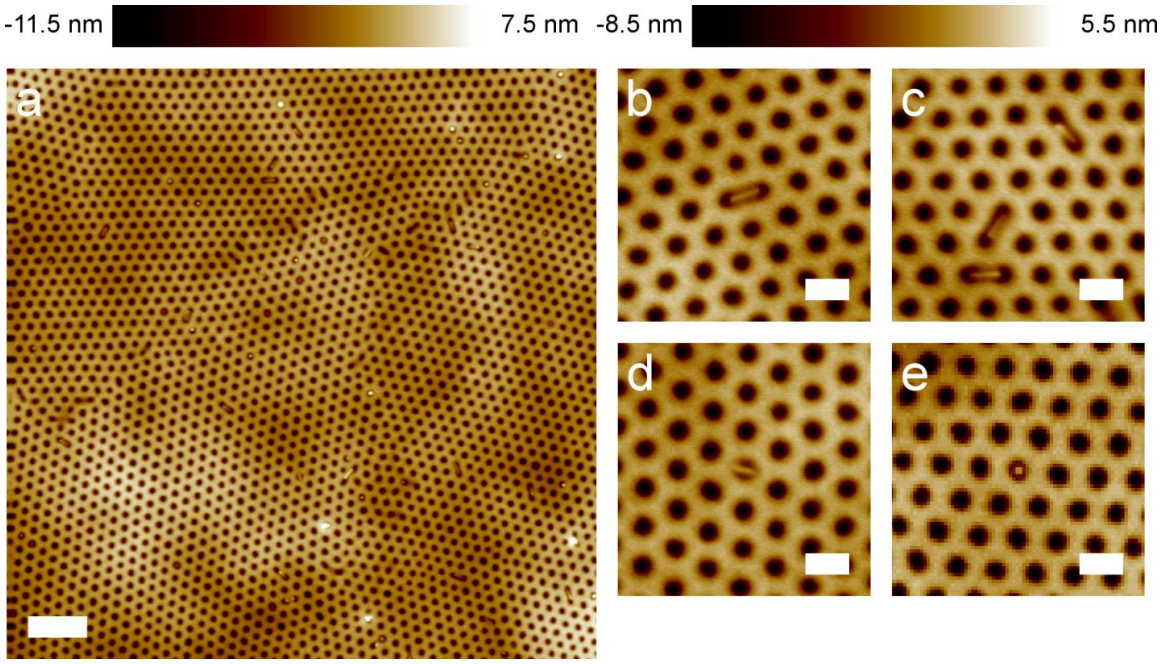

Figure 4.7. AFM topography images of the surface of PS-*b*-P2VP-AuNR70 films. (a) Large area AFM image showing AuNRs in the bridging and centered states. The image also shows a circular feature at the top of some vertical cylinders. The scale bar is 400 nm. (b) AFM image of an AuNR in the bridging state not at a defect in the vertical cylinder lattice. The scale bar is 100 nm. (c) AFM image of multiple AuNRs in the bridging state. The same AuNRs can be observed at the top middle of (a). The scale bar is 100 nm. (d) AFM image of an AuNR in the centered state not at a defect in the vertical cylinder lattice. The scale bar is 100 nm. (e) AFM image of a circular feature colocalized with a vertical P2VP cylinder. The scale bar is 100 nm.

As seen in Figure 4.7a, AFM topography images show AuNRs at the surface of the PS-*b*-P2VP-AuNR70 films. AuNRs in the bridging state are observed as shown in Figures 4.7a-c. AuNRs are also observed in the "centered state", which can be seen in

Figures 4.7a,d. The centered state is where an AuNR is positioned over a single P2VP cylinder, embedded in the film, and the long axis of the AuNR is parallel to the surface of the film. We found that 75% of AuNRs were in the bridging state and that 22% of AuNRs were in the centered state. Of the bridging AuNRs, 80% were not at a defect in the lattice and 77% of the centered AuNRs were not at a defect in the lattice. The definitions for bridging and centered AuNRs not at a defect in the lattice are given in the Methods. The 3% of AuNRs not in the centered or bridging states are embedded in the film surface and parallel to the film surface, however, the lattice around the AuNRs had so many defects that it could not be determined whether they were in a bridging, centered, or other state.

We analyzed AuNRs in the bridging state not at a defect in the lattice. The top of these AuNRs, measuring from the midpoint of the line defined by the crest of the AuNR, was on average 1.7 nm below the PS matrix. The average angle of the AuNRs long axis relative to the surface of the film was 2.3°, showing that the AuNRs were parallel to the film surface. Further, we found the region around the AuNRs to be on average 1.5 nm below the top of the AuNRs. Like the AuNRs in the bridging state not at a defect in the lattice, the AuNRs in the bridging state at a defect in the lattice were parallel to the film surface and had their tops below the film surface.

AuNRs in the centered state not at a defect in the lattice were analyzed. The AuNRs top, measuring from the midpoint of the line defined by the crest of the AuNR, was on average 0.6 nm below the PS matrix. The top of the AuNRs was essentially level with the PS matrix. The AuNRs were parallel to the film surface with an average angle of

1.8° between the long axis of the AuNRs and the surface of the film. AuNRs in the centered state at a defect in the lattice also had their tops level with the PS matrix and their long axis was parallel to the film surface.

The AFM images of the PS-*b*-P2VP-AuNR70 films also show that some vertical P2VP cylinders have a circular feature located at their top (Figure 4.7e). This was also observed for the PS-*b*-P2VP-AuNR101 films. As for the PS-*b*-P2VP-AuNR101 films, possible explanations for the circular features are that they are the end of a vertically oriented AuNR localized within a vertical P2VP cylinder or that they are a spherical nanoparticle localized within a vertical P2VP cylinder.

The PS-*b*-P2VP-AuNR70 films were further characterized with SEM. Top-down SEM images show that there are AuNRs at the surface of the films and these AuNRs are parallel to the surface of the film (Figure 4.8). Top-down SEM images also show circular features at the surface. The presence of parallel AuNRs and circular features at the surface matches our AFM results. Top-down SEM images also show that there are nanorods below the film surface that are not vertically oriented and that there are circular features below the film surface. The presence of nanorods below the film surface that are not vertically oriented indicates that there are nanorods below the film surface that are not localized within vertical P2VP cylinders. The circular features below the film surface could either be gold nanospheres or vertically oriented AuNRs.

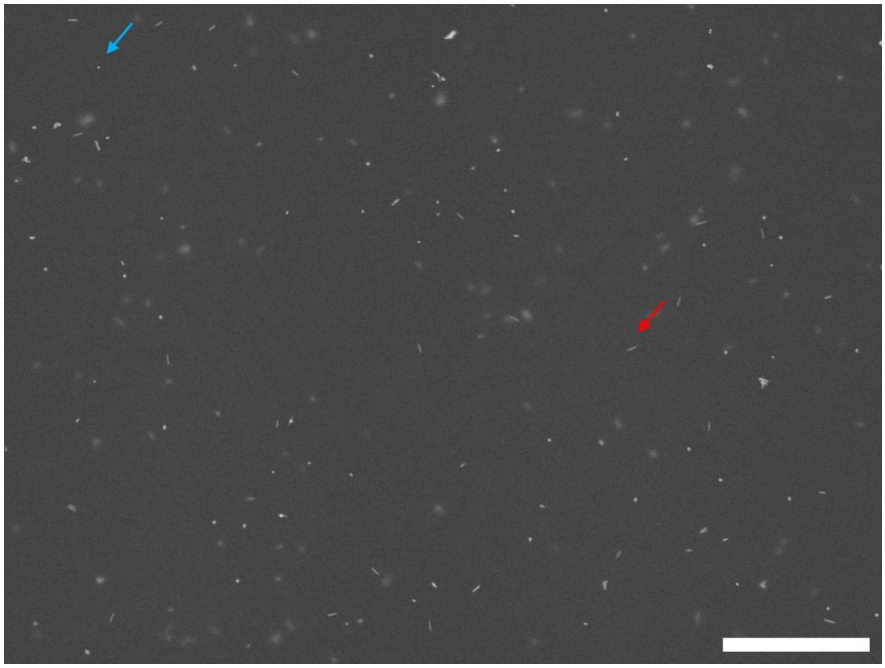

Figure 4.8. Top-down SEM image of a PS-*b*-P2VP-AuNR70 film. The red arrow points to a nanorod at the film surface that is parallel to the film surface. The blue arrow points to a circular feature at the film surface. The scale bar is 1 μm.

SEM images of the film cross-sections show vertically oriented AuNRs in the films with their top end at the film surface (blue arrow in Figure 4.9). In our AFM images we observed that some vertical cylinders had a circular feature at their top. Thus, we can conclude that the vertical AuNRs with their top end at the film surface are localized in vertical P2VP cylinders. AuNRs parallel to the film surface are also observed at the film surface in cross-sectional SEM images in agreement with our AFM results. In addition, circular features are observed at the film surface. These features could be attributed to an AuNR viewed end-on or a gold nanosphere. The cross-section SEM images show that inside the films AuNRs have many different orientations suggesting that these AuNRs are

not localized in vertical P2VP cylinders. Also observed inside the films are circular features which could be attributed to AuNRs being viewed end-on or gold nanospheres.

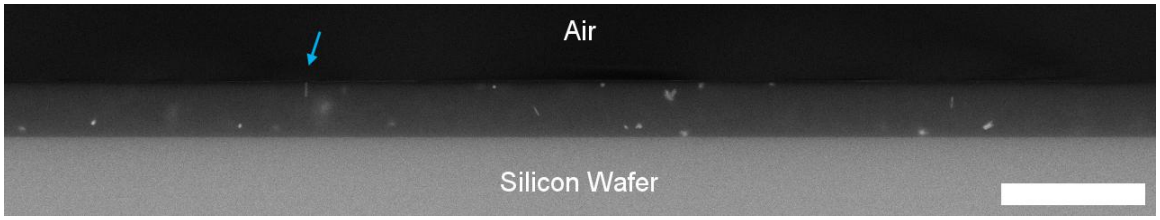

Figure 4.9. SEM image of the cross-section of a PS-*b*-P2VP-AuNR70 film. The blue arrow points to a vertically oriented AuNR with its tip at the surface of the film. The scale bar is 1 μm.

Hybrid Particle-Field Theory Simulations

AFM and SEM results showed that AuNRs at the surface of PS-*b*-P2VP-AuNR101 films are either bridging or vertical while AuNRs at the surface of PS-*b*-P2VP-AuNR70 films are either bridging, centered or vertical. To understand how AuNRs distribute between the bridging, centered and vertical states in the PS-*b*-P2VP-AuNR101 and PS-*b*-P2VP-AuNR70 films, HPFT simulations were performed. In the simulations a single nanorod was placed into a vertical cylinder diblock copolymer film representative of experimental films in either the bridging state, the centered state, or the vertical state and the free energy of the system was calculated. For each state, the free energy of the system was calculated as a function of nanorod length relative to the center-to-center distance between P2VP domains.

For the simulated neat diblock copolymer film, the vertical cylinders had a nearest-neighbor center-to-center distance r_{ctc} of 5.09 R_g and a diameter of 2.85 R_g, where R_g is the ideal radius of gyration of the diblock copolymer. The thickness of the HPFT simulation film was 9 R_g, which is sufficiently thick for the interfaces to not interact. For comparison in our experimental system the center-to-center distance between nearest-neighbor vertical cylinders was 6.03 $R_{g,exp}$, the cylinder diameter was 3.12 $R_{g,exp}$, and the film thickness was 26.36 $R_{g,exp}$ where $R_{g,exp}$ is the radius of gyration of PS(M_n = 180,000 g mol^{-1})-*b*-P2VP(M_n = 77,000 g mol^{-1}). Assuming Gaussian chain statistics with equal statistical segments sizes for both blocks, we calculate $R_{g,exp}$ = 13.8 nm using b_{exp} = 0.68 nm.[28] The difference in parameters in the calculations and the experiments is due to the difference in χ values expected in the experiments and employed in the simulations, which leads to a larger domain spacing relative to the neat polymer R_g.

Since in the experiments the AuNRs are densely functionalized with short P2VP ligands, in our HPFT simulations we model the nanorod as though it has the same chemistry as the minority block of the copolymer, resulting in an athermal nanorod-monomer interaction with the cylinder-forming block. The simulations were performed with a nanorod of 1 R_g diameter as this diameter is representative of the diameters of the AuNRs used in experiments (12 nm and 16 nm). In the experimental system in terms of $R_{g,exp}$ the diameter of the 12 nm diameter AuNRs was 0.87 $R_{g,exp}$ and the diameter of the 16 nm diameter AuNRs was 1.16 $R_{g,exp}$. For the bridging, centered, and vertical states, Figure 4.10 shows the system free energy, ΔF, as a function of nanorod length, L_{NR},

normalized by r_{ctc}. The free energy ΔF in k_BT is taken relative to the free energy of a vertical nanorod with a diameter and length of 1 R_g and 2 R_g, respectively.

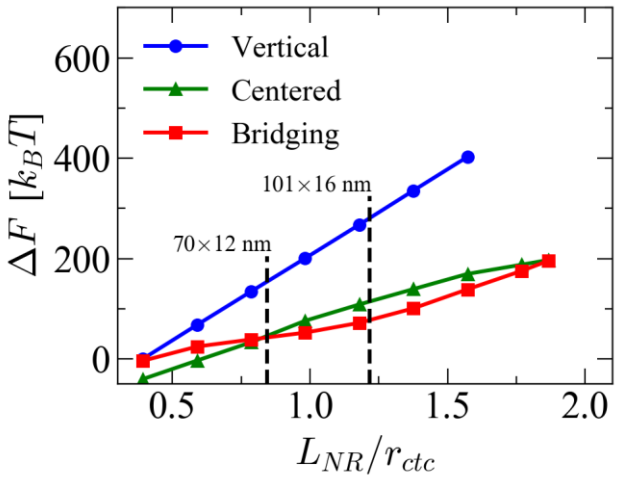

Figure 4.10. Free energy for nanorods of diameter 1 R_g in the bridging, centered, and vertical states as a function of nanorod length. The nanorod length, L_{NR}, is normalized by the vertical cylinder nearest-neighbor center-to-center distance, r_{ctc}. The free energy is taken relative to the free energy of a nanorod of diameter 1 R_g and length 2 R_g in the vertical state. The free energies for PS-*b*-P2VP-AuNR70 and PS-*b*-P2VP-AuNR101 films are denoted by vertical dashed lines.

The HPFT simulation predictions can be compared with the two experimental systems. For the PS-*b*-P2VP-AuNR101 experimental system L_{NR}/r_{ctc} = 1.22 (right vertical dashed line in Figure 4.10). At this L_{NR}/r_{ctc} Figure 4.10 shows that the bridging state is thermodynamically favored, while the centered state is less favorable and the vertical state is even more unfavorable. Using the Boltzmann distribution and interpolated values of ΔF at L_{NR}/r_{ctc} = 1.22 to estimate relative populations, HPFT

simulations predict that virtually all AuNRs should be in the bridging state, with negligible centered and vertical fractions of 8.7×10^{-17} and 2.9×10^{-89}. Comparing the HPFT simulations with the experimental horizontal states, only the bridging state is observed in PS-*b*-P2VP-AuNR101 films consistent with HPFT simulations. However, whereas HPFT simulations predict that the vertical state is unfavorable, experiments (*i.e.*, AFM and SEM) show that there are AuNRs in the vertical state in PS-*b*-P2VP-AuNR101 films. This could be due to fluctuation effects that are neglected in the HPFT simulation calculations, or it could be a result of the solvent annealing processing used to generate the experimental systems.

For PS-*b*-P2VP-AuNR70 films $L_{NR}/r_{ctc} = 0.84$ (left vertical dashed line in Figure 4.10). At $L_{NR}/r_{ctc} = 0.84$ Figure 4.10 shows that the bridging state is slightly more favored than the centered state and the vertical state is the least thermodynamically favored state. Using the Boltzmann distribution and ΔF at $L_{NR}/r_{ctc} = 0.84$ to estimate relative populations, we expect a non-negligible fraction of centered nanorods, where the ratio of bridging to centered nanorods is about 12:1. The vertical state is again expected to be negligible with a vertical fraction of about 1.3×10^{-48}. In PS-*b*-P2VP-AuNR70 films, AuNRs are observed in the bridging, the centered and the vertical state with the ratio of the bridging to centered states being 3.5:1. It is important to note that this ratio is the ratio of bridging rods away from defects to centered rods away from defects as previously discussed. The simulation results trend in a similar direction with the experiments in that the centered state is more preferable for the shorter nanorods than for the longer ones. However, the results are not in quantitative agreement with the experiments.

In addition to the results with a nanorod diameter of 1 R_g (Figure 4.10), HPFT simulations were used to calculate the free energy for thicker nanorods, with diameters of 1.5 R_g and 2 R_g as shown in Figures A.8b and c, respectively. Briefly, we find that the range of L_{NR}/r_{ctc} where bridging is favored grows with increasing diameter, and the range where centered is favored decreases.

There are several possible explanations for the differences between experiments and HPFT simulation predictions. First, nanocomposite films were processed *via* solvent annealing where the BCP and the AuNRs co-assemble during swelling and solvent evaporation. As a result, AuNRs in the dry film may be kinetically trapped in thermodynamically unfavorable or metastable states.[29] Due to the mean-field nature of the calculations, these kinetic effects are not represented in the simulations. Second, the simulations do not explicitly model the grafted polymers, and therefore these calculations would not capture any entropy associated with the grafted polymers that may be important. Finally, the experimental χN parameter is larger than those used in the simulations and we have assumed equal interactions (surface energy) of both blocks with the top surface.

Simulations were also used to reveal the morphology of the BCP when a nanorod is in the bridging state. Figures 4.11a,b show the 3D field configuration and a 2D slice along the length of the nanorod for a nanorod in the bridging state with diameter and length of 1 R_g and 6 R_g. These nanorod dimensions approximately correspond to the 101 nm length by 16 nm diameter AuNRs in the PS-*b*-P2VP-AuNR101 films. Both representations show that minority blocks wet the underside of the bridging nanorod

resulting in the two bridged vertical cylinders becoming connected into one arch shaped domain. The vertical cylinders forming each "column" of the arch remain intact. Characterization of the wetting layer is not experimentally accessible, emphasizing the importance of using HPFT simulations to interpret experimental results. In summary, HPFT simulations reveal that when an AuNR bridges two vertical cylinders that the domains remain intact below the surface and a wetting layer is formed beneath the nanorod.

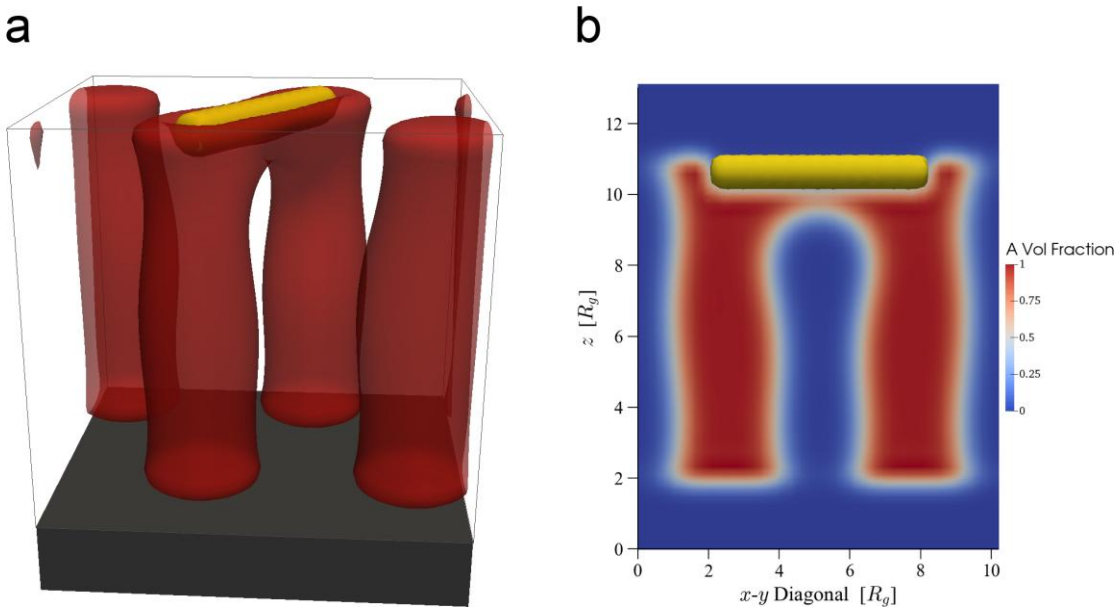

Figure 4.11. For a nanorod of diameter 1 R_g and length 6 R_g in the bridging state (a) shows the isosurface (red) of 0.5 local volume fraction of block A and (b) shows the local A block volume fraction in a 2D slice along the length of the nanorod. The A block is the cylinder forming block.

4.4 Conclusions

The ability to control the position and orientation of nanorods at the surface of self-assembled vertical block copolymer cylinder-nanorod nanocomposites is demonstrated. The longer nanorods either bridge vertical cylinders at the surface or are localized within vertical cylinders with their tip at the film surface. In addition to the two states assumed by the longer nanorods, shorter nanorods assume a state where they are centered at the top of one vertical cylinder. HPFT simulations provided the relative free energies of the three states as a function of nanorod length and provided insight into the polymer morphology when a nanorod was in the bridging state. The bridging state observed in this work has many potential applications in self-assembled nanoscale devices. Further, to our knowledge this work demonstrates the first example of controlling nanoparticle position and orientation in a BCP via the bridging of two domains separated by a third domain. This is a promising approach for developing new devices and materials with desired properties.

4.5 Methods

Synthesis of 101 nm Length by 16 nm Diameter AuNRs. The AuNRs were synthesized according to Ye *et al.*[30] The AuNRs were imaged with transmission electron microscopy (TEM) (JEOL JSM-7500F Field Emission Scanning Electron Microscope, Transmission Electron Detector) and the nanorod dimensions were determined from the TEM images (Figure A.4). The AuNRs were also characterized with UV-vis-NIR spectroscopy (Figure A.5) (Varian Cary 5000 UV-Vis-NIR Spectrophotometer).

Preparation and Characterization of Neat Vertical Cylinder PS-*b*-P2VP Films. Neat vertical cylinder PS-*b*-P2VP films were prepared following Yin *et al.*[23] A 2 wt % PS(M_n = 180,000 g mol^{-1})-*b*-P2VP(M_n = 77,000 g mol^{-1})(PDI = 1.09) (Polymer Source. Inc.) solution in chloroform was prepared and spin-coated on silicon wafers at 2000 rpm for 30 s. The resulting film was characterized with tapping mode AFM (Bruker Dimension Icon). The silicon wafer was then placed on a stand in a glass jar with the stand surrounded by a pool of chloroform. The jar was firmly sealed with its lid and the film was left to solvent anneal for the desired time. Subsequently, the lid of the jar was removed and the wafer piece removed. Films were solvent annealed for 7:30, 10:00, 11:15, 12:30, 13:45, 14:23, 15:00, 16:15, 17:30 where the first number in the format x:y is minutes and the second number is seconds. The solvent annealed films were characterized with AFM in tapping mode.

Films solvent annealed for 14:23 were imaged with SEM. For SEM imaging solvent annealed films were stained with iodine. A film was stained with iodine by placing it in a jar with iodine, sealing the jar, and placing the jar in an oven at 50 °C for 3 hours. The films were imaged top-down with SEM (JEOL JSM-7500F Field Emission Scanning Electron Microscope) using the Low Angle Backscatter (LABe) detector. The wafers supporting the iodine stained films were also cleaved in two and the film cross-sections were imaged with SEM using the LABe detector.

Preparation and Characterization of PS-*b*-P2VP-AuNR101 and PS-*b*-P2VP-AuNR70 Nanocomposite Films. PS-*b*-P2VP-AuNR101 and PS-*b*-P2VP-AuNR70 nanocomposite films were prepared and characterized the same way except PS-*b*-P2VP-

AuNR101 nanocomposite films were prepared with the synthesized 101 nm length by 16 nm diameter AuNRs while PS-*b*-P2VP-AuNR70 nanocomposite films were prepared with 70 nm length by 12 nm diameter AuNRs purchased from nanoComposix, Inc. (surface: sodium citrate).

Nanocomposite films were prepared as follows. A solution of AuNRs in water was centrifuged at 9289*g* for 30 minutes (Eppendorf Centrifuge 5804). The supernatant was removed and the concentrated AuNRs at the bottom of the centrifuge tube were added to a 10 ml solution of P2VP-SH (M_n = 2500 g mol^{-1}, PDI = 1.16) (Polymer Source. Inc.) in N,N-dimethylformamide (DMF) while the solution was stirring. The solution was then stirred overnight. The solution was subsequently centrifuged at 9289*g* for 30 minutes and the supernatant removed. 10 ml of DMF was then added to the centrifuge tube and the AuNRs were resuspended. The solution was then transferred to a new centrifuge tube and centrifuged at 9289*g* for 30 minutes. The supernatant was removed and 10 ml of DMF was added. The AuNRs were resuspended and the solution was transferred to a new centrifuge tube. The solution was then centrifuged at 9289*g* for 30 minutes and the supernatant was removed. The concentrated AuNRs at the bottom of the centrifuge tube were then added to a stirring 1 ml 2 wt % PS(M_n = 180,000 g mol^{-1})-*b*-P2VP(M_n = 77,000 g mol^{-1})(PDI = 1.09) in chloroform solution and the solution was stirred for 2 hours. The solution was subsequently spin-coated on silicon wafers at 2000 rpm for 30 s. The films were solvent annealed in chloroform for 14 minutes 23 seconds in an identical fashion to the neat films. The surfaces of the solvent annealed films were characterized with AFM in tapping mode. The solvent annealed films were also

characterized with SEM top-down using the LABe detector. The films' cross-sections were imaged with SEM using the LABe detector by cleaving the wafers supporting the films in half.

Definition of an AuNR Away From Defects in the Vertical Cylinder Lattice. For an AuNR in the bridging state we define the AuNR as away from defects in the vertical cylinder lattice as follows. Given a perfect hexagonal lattice of vertical cylinders with an AuNR in the bridging state we take the two vertical cylinders being bridged by the AuNR and which are colored red in Figure A6. We then take the nearest neighbor cylinders of the two red cylinders, which are colored green in Figure A6. Finally, we take the nearest neighbor cylinders of the green cylinders, which are colored blue in Figure A6. For an experimentally observed AuNR in the bridging state if the vertical cylinder lattice around the AuNR does not deviate substantially from the perfect hexagonal lattice in the region of the lattice corresponding to the green and blue cylinders, the AuNR is away from defects in the lattice.

For an AuNR in the centered state we defined it as away from defects in the vertical cylinder lattice as follows. Given a perfect hexagonal lattice of vertical cylinders with an AuNR in the centered state we take the vertical cylinder into the top of which the AuNR is embedded, colored red in Figure A.7. We then take the nearest neighbor cylinders of the red cylinder, which are colored green in Figure A.7. Then we take the nearest neighbor cylinders of the green cylinders, which are colored blue in Figure A.7. For an experimentally observed AuNR in the centered state if the vertical cylinder lattice around the AuNR does not deviate substantially from the perfect hexagonal lattice in the

region of the lattice corresponding to the green and blue cylinders, the AuNR is away from defects in the lattice.

Hybrid Particle-Field Theory Simulations. HPFT is a framework developed by Sides *et al.*[31] in which particles are treated as fixed cavity functions and mean-field polymer distributions are calculated around them. Our mean-field HPFT simulations consisted of an A-B diblock copolymer and an explicit nanorod confined between two neutral surfaces in a weakly compressible system. The diblock chain was modeled as a discrete Gaussian chain of length $N = 60$ segments and was biased by an initial field configuration to form vertical cylinders. The nanorod was modeled as a fixed, bare, A-like particle. The enthalpic repulsion between A and B segments was set to $\chi N = 30$. Polymer free energy differences between different states (particle diameter, length, and orientation) was calculated from differences in the effective Hamiltonian. More complete details of the model parameters and equations are given in the Supporting Information.

4.6 Material in Appendix A

AFM images of neat as-spin-coated PS-*b*-P2VP films; AFM images of neat PS-*b*-P2VP films solvent annealed for various lengths of time; TEM image of the 101 nm length by 16 nm diameter AuNRs; UV-vis-NIR spectrum of the 101 nm length by 16 nm diameter AuNRs; diagram for identifying that a bridging AuNR is not at a defect in the hexagonal lattice; diagram for identifying that a centered AuNR is not at a defect in the hexagonal lattice; HPFT simulation results for 1.5 R_g and 2 R_g diameter nanorods; additional model details

4.7 References

1. Maier, S. A.; Kik, P. G.; Atwater, H. A.; Meltzer, S.; Harel, E.; Koel, B. E.; Requicha, A. A. G., Local Detection of Electromagnetic Energy Transport Below the Diffraction Limit in Metal Nanoparticle Plasmon Waveguides. *Nat Mater* **2003,** *2* (4), 229-232.

2. Abetz, V.; Simon, P. F. W., Phase Behaviour and Morphologies of Block Copolymers. In *Block Copolymers I*, Abetz, V., Ed. Springer Berlin Heidelberg: Berlin, Heidelberg, 2005; pp 125-212.

3. Bockstaller, M. R.; Mickiewicz, R. A.; Thomas, E. L., Block Copolymer Nanocomposites: Perspectives for Tailored Functional Materials. *Adv Mater* **2005,** *17* (11), 1331-1349.

4. Kao, J.; Thorkelsson, K.; Bai, P.; Rancatore, B. J.; Xu, T., Toward Functional Nanocomposites: Taking the Best of Nanoparticles, Polymers, and Small Molecules. *Chem Soc Rev* **2013,** *42* (7), 2654-2678.

5. Chiu, J. J.; Kim, B. J.; Kramer, E. J.; Pine, D. J., Control of Nanoparticle Location in Block Copolymers. *J Am Chem Soc* **2005,** *127* (14), 5036-5037.

6. Kim, B. J.; Bang, J.; Hawker, C. J.; Kramer, E. J., Effect of Areal Chain Density on the Location of Polymer-Modified Gold Nanoparticles in a Block Copolymer Template. *Macromolecules* **2006,** *39* (12), 4108-4114.

7. Kim, B. J.; Fredrickson, G. H.; Kramer, E. J., Effect of Polymer Ligand Molecular Weight on Polymer-Coated Nanoparticle Location in Block Copolymers. *Macromolecules* **2008,** *41* (2), 436-447.

8. Bockstaller, M. R.; Lapetnikov, Y.; Margel, S.; Thomas, E. L., Size-Selective Organization of Enthalpic Compatibilized Nanocrystals in Ternary Block Copolymer/Particle Mixtures. *J Am Chem Soc* **2003,** *125* (18), 5276-5277.

9. Lin, Y.; Boker, A.; He, J. B.; Sill, K.; Xiang, H. Q.; Abetz, C.; Li, X. F.; Wang, J.; Emrick, T.; Long, S.; Wang, Q.; Balazs, A.; Russell, T. P., Self-Directed Self-Assembly of Nanoparticle/Copolymer Mixtures. *Nature* **2005,** *434* (7029), 55-59.

10. Kang, H.; Detcheverry, F. A.; Mangham, A. N.; Stoykovich, M. P.; Daoulas, K. C.; Hamers, R. J.; Muller, M.; de Pablo, J. J.; Nealey, P. F., Hierarchical Assembly of Nanoparticle Superstructures from Block Copolymer-Nanoparticle Composites. *Phys Rev Lett* **2008,** *100* (14).

11. Zhao, Y.; Thorkelsson, K.; Mastroianni, A. J.; Schilling, T.; Luther, J. M.; Rancatore, B. J.; Matsunaga, K.; Jinnai, H.; Wu, Y.; Poulsen, D.; Frechet, J. M. J.;

Alivisatos, A. P.; Xu, T., Small-Molecule-Directed Nanoparticle Assembly Towards Stimuli-Responsive Nanocomposites. *Nat Mater* **2009,** *8* (12), 979-985.

12. Deshmukh, R. D.; Liu, Y.; Composto, R. J., Two-Dimensional Confinement of Nanorods in Block Copolymer Domains. *Nano Lett* **2007,** *7* (12), 3662-3668.

13. Thorkelsson, K.; Mastroianni, A. J.; Ercius, P.; Xu, T., Direct Nanorod Assembly Using Block Copolymer-Based Supramolecules. *Nano Lett* **2012,** *12* (1), 498-504.

14. Thorkelsson, K.; Nelson, J. H.; Alivisatos, A. P.; Xu, T., End-to-End Alignment of Nanorods in Thin Films. *Nano Lett* **2013,** *13* (10), 4908-4913.

15. Thorkelsson, K.; Bronstein, N.; Xu, T., Nanorod-Based Supramolecular Nanocomposites: Effects of Nanorod Length. *Macromolecules* **2016,** *49* (17), 6669-6677.

16. Halevi, A.; Halivni, S.; Oded, M.; Muller, A. H. E.; Banin, U.; Shenhar, R., Co-Assembly of a-B Diblock Copolymers with B'-Type Nanoparticles in Thin Films: Effect of Copolymer Composition and Nanoparticle Shape. *Macromolecules* **2014,** *47* (9), 3022-3032.

17. Ploshnik, E.; Salant, A.; Banin, U.; Shenhar, R., Hierarchical Surface Patterns of Nanorods Obtained by Co-Assembly with Block Copolymers in Ultrathin Films. *Adv Mater* **2010,** *22* (25), 2774-2779.

18. Ploshnik, E.; Salant, A.; Banin, U.; Shenhar, R., Co-Assembly of Block Copolymers and Nanorods in Ultrathin Films: Effects of Copolymer Size and Nanorod Filling Fraction. *Phys Chem Chem Phys* **2010,** *12* (38), 11885-11893.

19. Rasin, B.; Chao, H. K.; Jiang, G. Q.; Wang, D. L.; Riggleman, R. A.; Composto, R. J., Dispersion and Alignment of Nanorods in Cylindrical Block Copolymer Thin Films. *Soft Matter* **2016,** *12* (7), 2177-2185.

20. Breen, C. A.; Deng, T.; Breiner, T.; Thomas, E. L.; Swager, T. M., Polarized Photoluminescence from Poly(P-Phenylene-Ethynylene) Via a Block Copolymer Nanotemplate. *J Am Chem Soc* **2003,** *125* (33), 9942-9943.

21. Krook, N. M.; Ford, J.; Marechal, M.; Rannou, P.; Meth, J. S.; Murray, C. B.; Composto, R. J., Alignment of Nanoplates in Lamellar Diblock Copolymer Domains and the Effect of Particle Volume Fraction on Phase Behavior. *Acs Macro Lett* **2018,** *7* (12), 1400-1407.

22. Hsu, S. W.; Xu, T., Tailoring Co-Assembly of Nanodiscs and Block Copolymer-Based Supramolecules by Manipulating Interparticle Interactions. *Macromolecules* **2019,** *52* (7), 2833-2842.

23. Yin, J.; Yao, X. P.; Liou, J. Y.; Sun, W.; Sun, Y. S.; Wang, Y., Membranes with Highly Ordered Straight Nanopores by Selective Swelling of Fast Perpendicularly Aligned Block Copolymers. *Acs Nano* **2013,** *7* (11), 9961-9974.

24. Gu, X. D.; Gunkel, I.; Hexemer, A.; Gu, W. Y.; Russell, T. P., An in Situ Grazing Incidence X-Ray Scatterings Study of Block Copolymer Thin Films During Solvent Vapor Annealing. *Adv Mater* **2014,** *26* (2), 273-281.

25. Gu, X. D.; Gunkel, I.; Hexemer, A.; Russell, T. P., Controlling Domain Spacing and Grain Size in Cylindrical Block Copolymer Thin Films by Means of Thermal and Solvent Vapor Annealing. *Macromolecules* **2016,** *49* (9), 3373-3381.

26. Berezkin, A. V.; Papadakis, C. M.; Potemkin, I. I., Vertical Domain Orientation in Cylinder-Forming Diblock Copolymer Films Upon Solvent Vapor Annealing. *Macromolecules* **2016,** *49* (1), 415-424.

27. Elbs, H.; Krausch, G., Ellipsometric Determination of Flory-Huggins Interaction Parameters in Solution. *Polymer* **2004,** *45* (23), 7935-7942.

28. Tanaka, K.; Takahara, A.; Kajiyama, T., Film Thickness Dependence of the Surface Structure of Immiscible Polystyrene/Poly(Methyl Methacrylate) Blends. *Macromolecules* **1996,** *29* (9), 3232-3239.

29. Chao, H. K.; Koski, J.; Riggleman, R. A., Solvent Vapor Annealing in Block Copolymer Nanocomposite Films: A Dynamic Mean Field Approach. *Soft Matter* **2017,** *13* (1), 239-249.

30. Ye, X. C.; Zheng, C.; Chen, J.; Gao, Y. Z.; Murray, C. B., Using Binary Surfactant Mixtures to Simultaneously Improve the Dimensional Tunability and Monodispersity in the Seeded Growth of Gold Nanorods. *Nano Lett* **2013,** *13* (2), 765-771.

31. Sides, S. W.; Kim, B. J.; Kramer, E. J.; Fredrickson, G. H., Hybrid Particle-Field Simulations of Polymer Nanocomposites. *Phys Rev Lett* **2006,** *96* (25), 250601.

CHAPTER 5: Conclusions and Future Work

5.1 Conclusions

In this thesis the position and orientation of nanorods in vertical cylinder block copolymer (BCP) films is studied. The specific system investigated is films of cylinder forming polystyrene-*block*-poly(2-vinylpyridine) (PS-b-P2VP) and P2VP functionalized gold nanorods (AuNRs). When the system is solvent annealed the BCP assumes a morphology of vertical P2VP cylinders in a PS matrix.

When very short AuNRs are utilized, the AuNRs are found to localize in vertical cylinders near the substrate and are oriented parallel to the substrate. Simulations of this system show that the AuNRs localize at the base of the vertical cylinders to alleviate chain stretching. Simulations also showed that if the AuNR length was increased, the AuNRs would orient vertically inside the vertical P2VP cylinders.

When much longer 70 nm AuNRs were used in much thicker films, the AuNRs were distributed between three states at the surface of the films. The AuNRs were found in the bridging, centered and vertical states. The bridging state is where the AuNR is embedded in the film, its long axis is parallel to the film surface and each end of the AuNR is at the top of nearest neighbor vertical cylinders. The centered state is where the AuNR is embedded in the film surface, its long axis is parallel to the film surface and the AuNR is centered over one P2VP cylinder. The vertical state is where the AuNR is localized within a vertical P2VP cylinder, the AuNR is vertically oriented, and the tip of

the AuNR is at the film surface. When even longer 101 nm AuNRs are used the AuNRs are only found in the bridging and vertical states at the surface of the film. For both the 70 nm long AuNRs and the 101 nm long AuNRs, inside the film, away from the surface, the AuNRs are not found to assume a particular position or orientation. HPFT simulations were used to calculate the system free energy for the bridging, centered and vertical states as nanorod length was varied. The experimental distribution of nanorods between the bridging, centered and vertical states was compared to the distribution predicted by the HPFT simulations. HPFT simulations were also used to understand the BCP morphology when a 101 nm long AuNR was in the bridging state.

The studies in this thesis increase our understanding of anisotropic nanoparticle-block copolymer self-assembly. This will allow for better control over nanoparticle position and orientation in polymer nanocomposites and thus materials with improved properties.

5.2 Future Work

Bridging via Deposition of AuNRs on the Film Surface

Our studies with 101 nm long AuNRs show that while the AuNRs are distributed between the bridging and vertical states at the film surface, in the film the AuNRs have no particular orientation. From an engineering perspective we are not controlling the position and orientation of these nanorods. Thus, it would be desirable to obtain the bridging and vertical states at the surface of the film without having the AuNRs inside the film. A potential approach to do this is to deposit P2VP functionalized AuNRs onto the

surface of a PS-b-P2VP film that has not yet been solvent annealed. Subsequently, the film is solvent annealed and the goal is for the AuNRs at the surface to assume either the bridging or vertical states. Experiments have been conducted for this study.

16 nm diameter and 101 nm long AuNRs were functionalized with P2VP thiol. These P2VP functionalized AuNRs were in chloroform. A small dish was filled with water. The solution of AuNRs in chloroform was gently added dropwise onto the surface of the water in the dish. The AuNRs formed a layer on the water surface. A neat PS-*b*-P2VP film was dipped vertically in and out of the water resulting in the AuNRs being deposited onto the PS-*b*-P2VP film surface. The AuNRs formed 2D islands on the PS-*b*-P2VP film surface (Figure 5.1). We did not proceed with solvent annealing these nanocomposite films as for our proposed study individually dispersed AuNRs on the film surface are desirable.

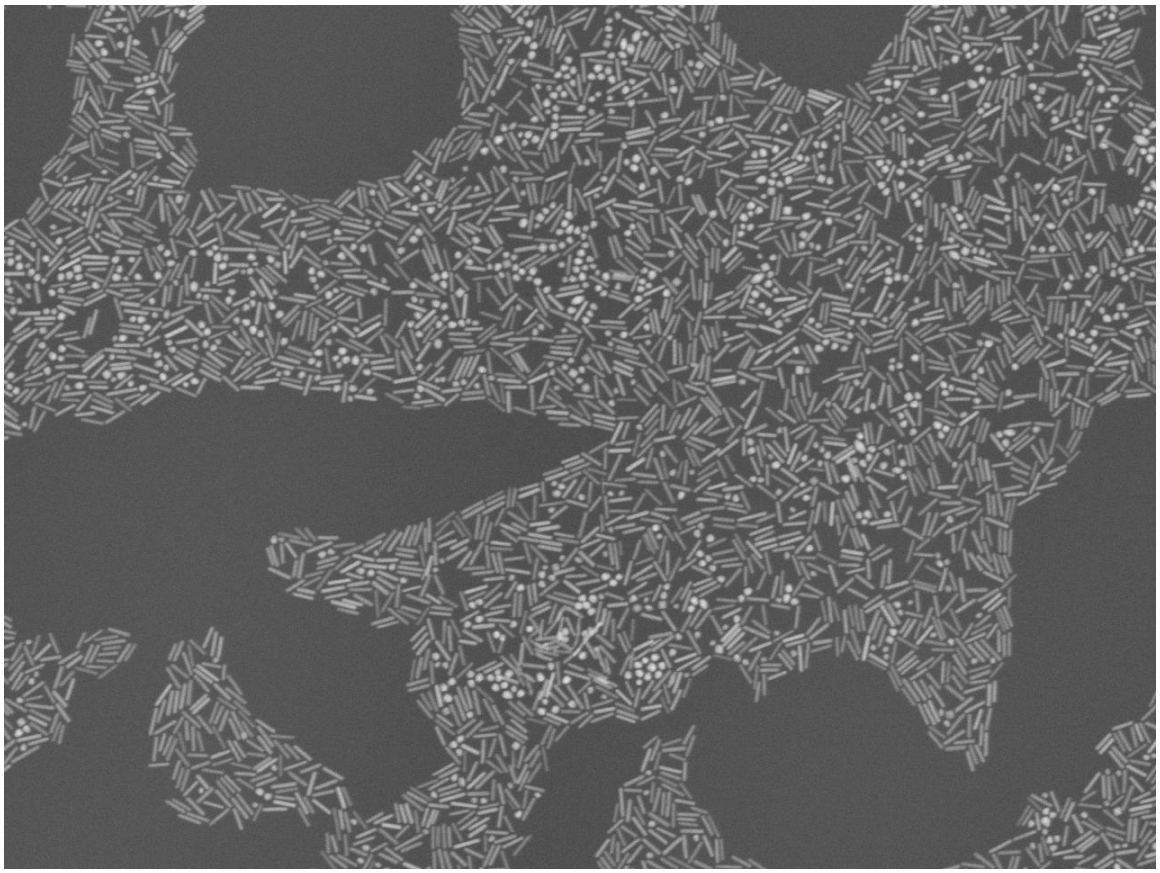

Figure 5.1. SEM image of a PS-*b*-P2VP film with P2VP functionalized AuNRs deposited on the film surface.

We also attempted to deposit P2VP functionalized AuNRs on PS-*b*-P2VP films with PDMS stamping. 101 nm long by 16 nm diameter AuNRs functionalized with P2VP were deposited from chloroform onto flat PDMS stamps. The stamps were allowed to dry and PS-*b*-P2VP films were stamped. We found that very few AuNRs transferred from the stamps to the PS-*b*-P2VP film surface.

Self-Assembly with Thin Nanorods

In our studies we do not obtain a nanocomposite structure where the nanorods are exclusively localized within vertical P2VP cylinders and are vertically oriented. A hypothesis for why this does not occur for the 70 nm long and 101 nm long AuNRs is that they are too thick. Incorporating these AuNRs into a cylinder causes to much of a conformational entropy penalty. Thus, it is hypothesized that if thinner nanorods were used, the conformational entropy penalty would be lower, and the nanorods would localize within the vertical P2VP cylinders with a vertical orientation.

APPENDIX A

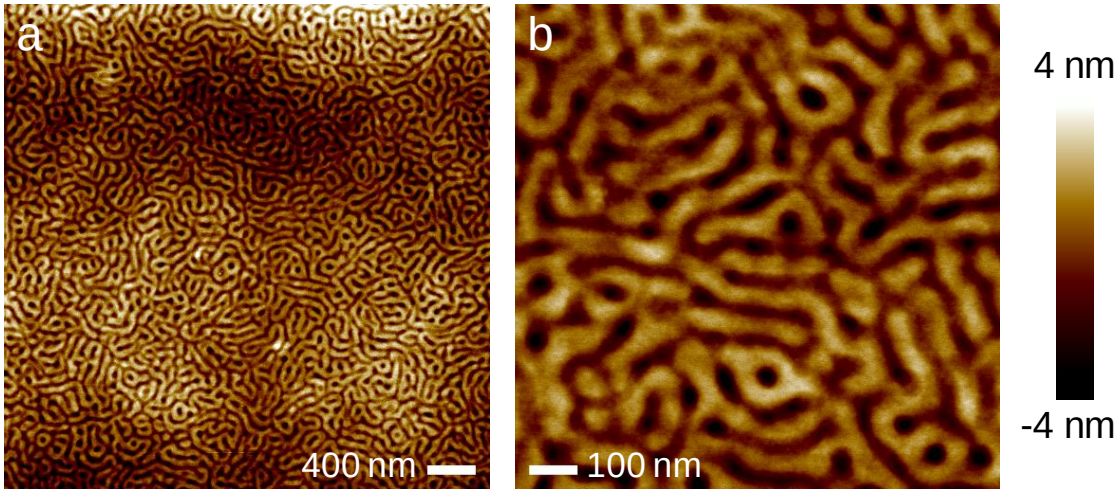

Figure A.1. AFM topography images of neat as-spin-coated PS-*b*-P2VP films. (a) shows a 4 µm by 4 µm AFM topography image and (b) shows a 1 µm by 1 µm AFM topography image.

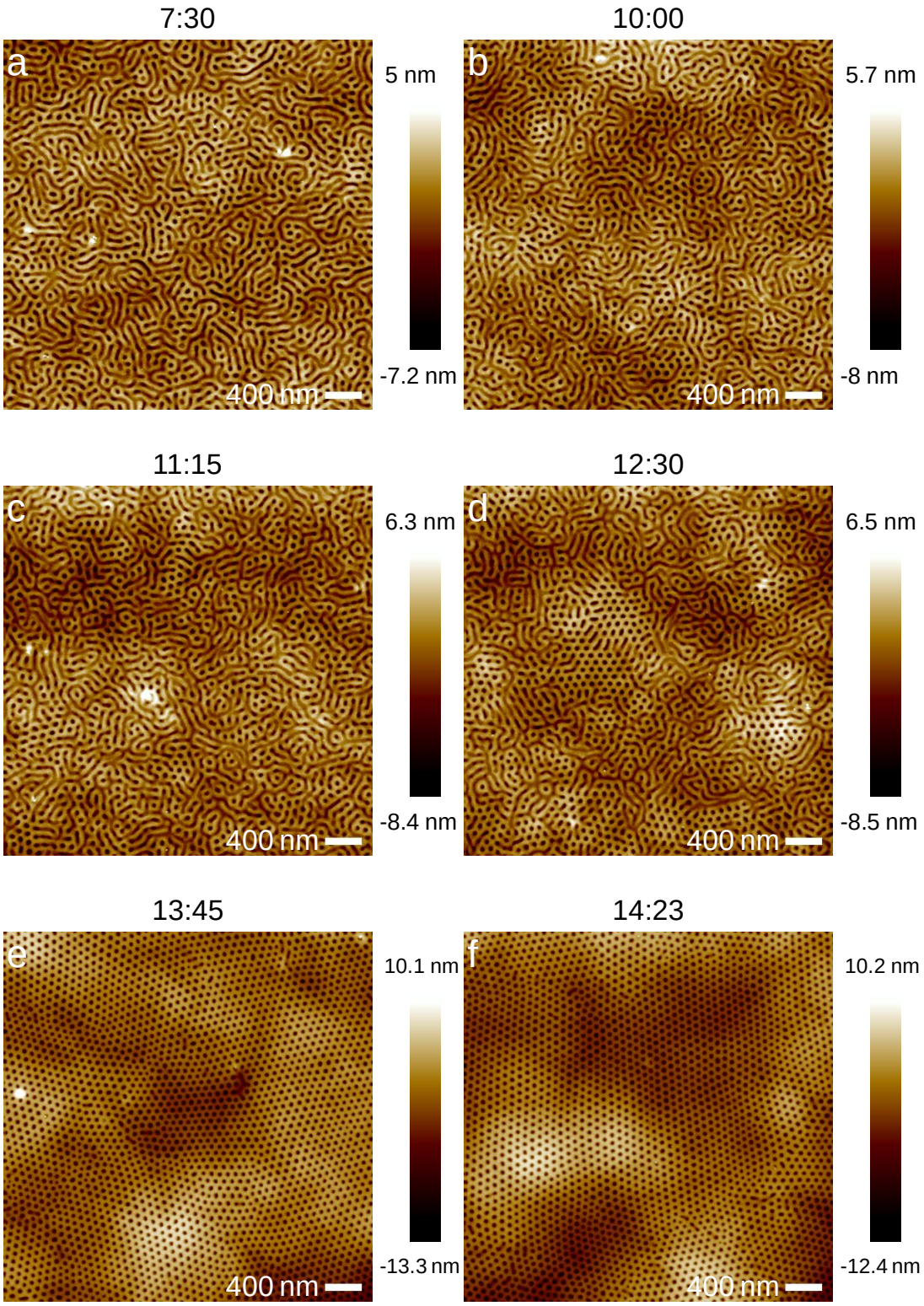
7:30
a
5 nm
-7.2 nm
400 nm
10:00
b
5.7 nm
-8 nm
400 nm
11:15
c
6.3 nm
-8.4 nm
400 nm
12:30
d
6.5 nm
-8.5 nm
400 nm
13:45
e
10.1 nm
-13.3 nm
400 nm
14:23
f
10.2 nm
-12.4 nm
400 nm

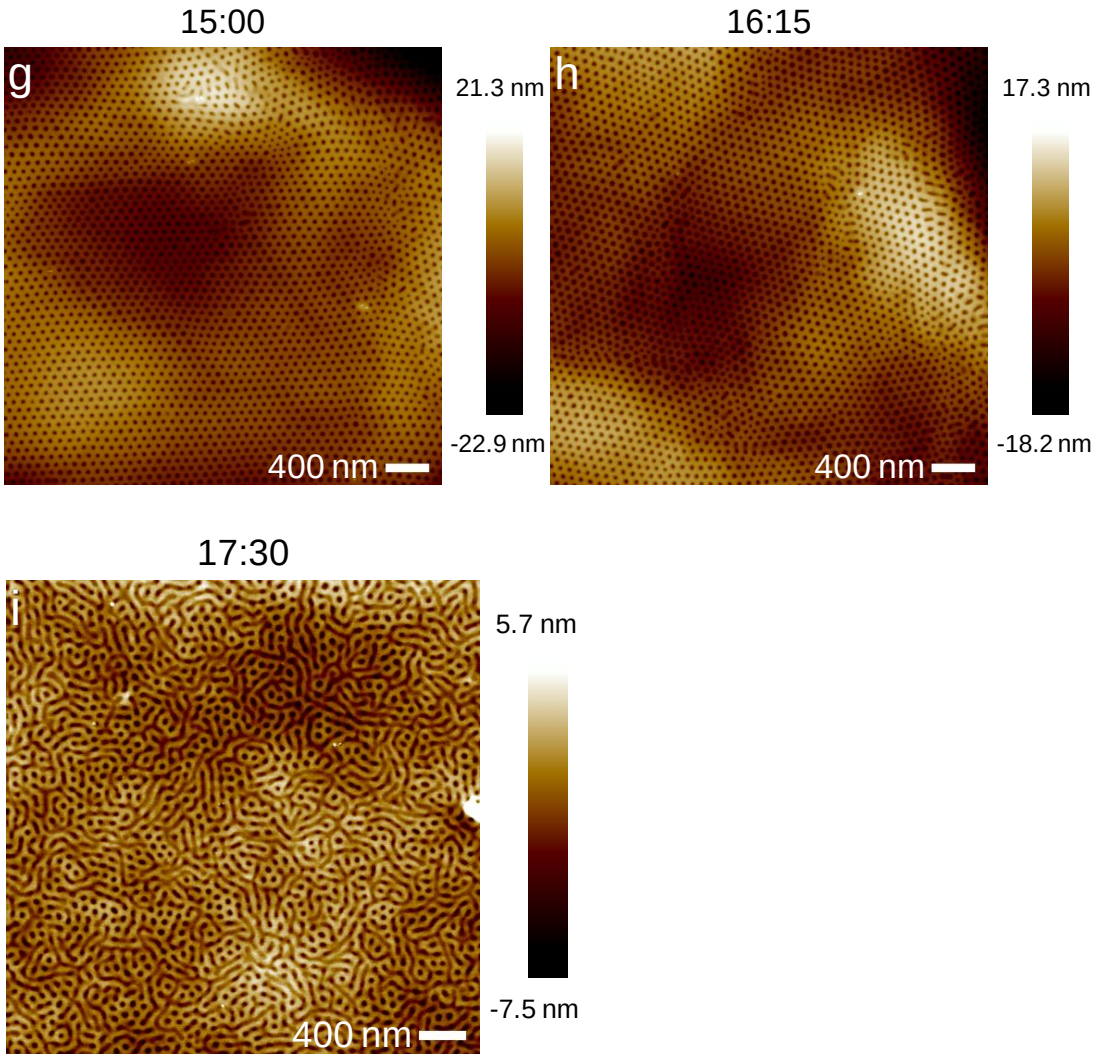

Figure A.2. AFM topography images of neat PS-*b*-P2VP films solvent annealed in chloroform for various lengths of time. Above each AFM image the length of time the film in the image was solvent annealed is indicated in the format minutes:seconds.

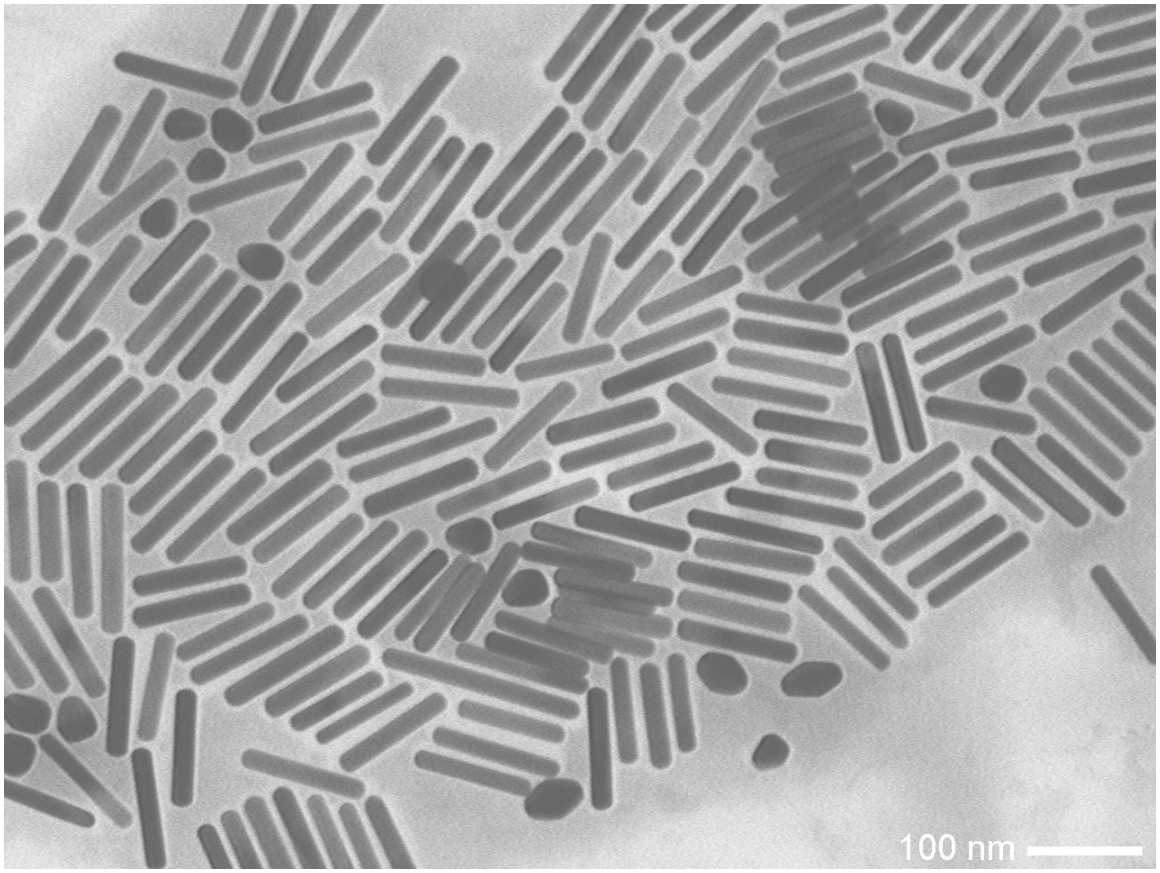

Figure A.4. TEM image of the 101 nm length by 16 nm diameter gold nanorods.

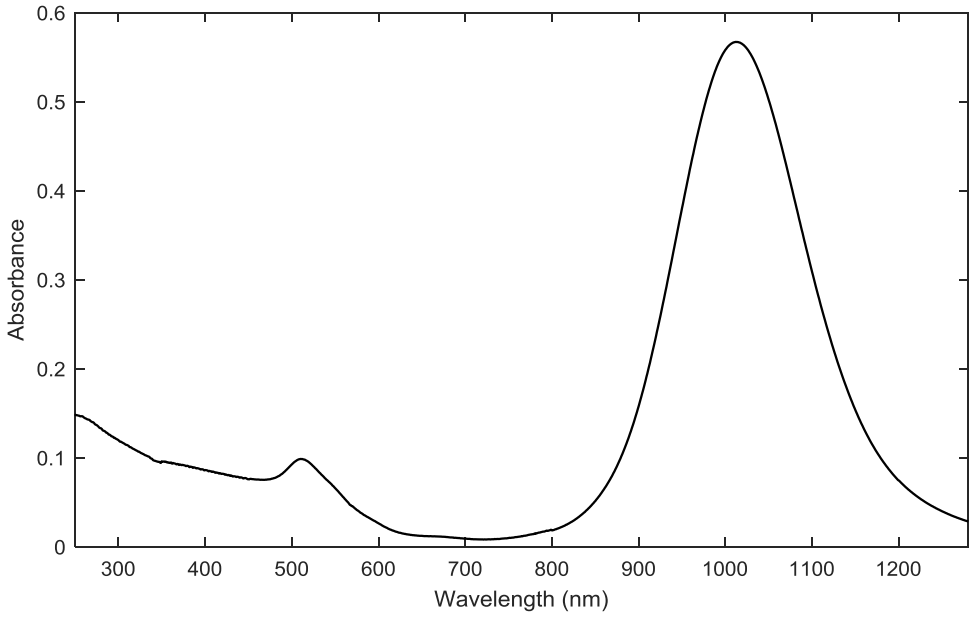

Figure A.5. UV-vis-NIR spectrum of the 101 nm length by 16 nm diameter gold nanorods in water.

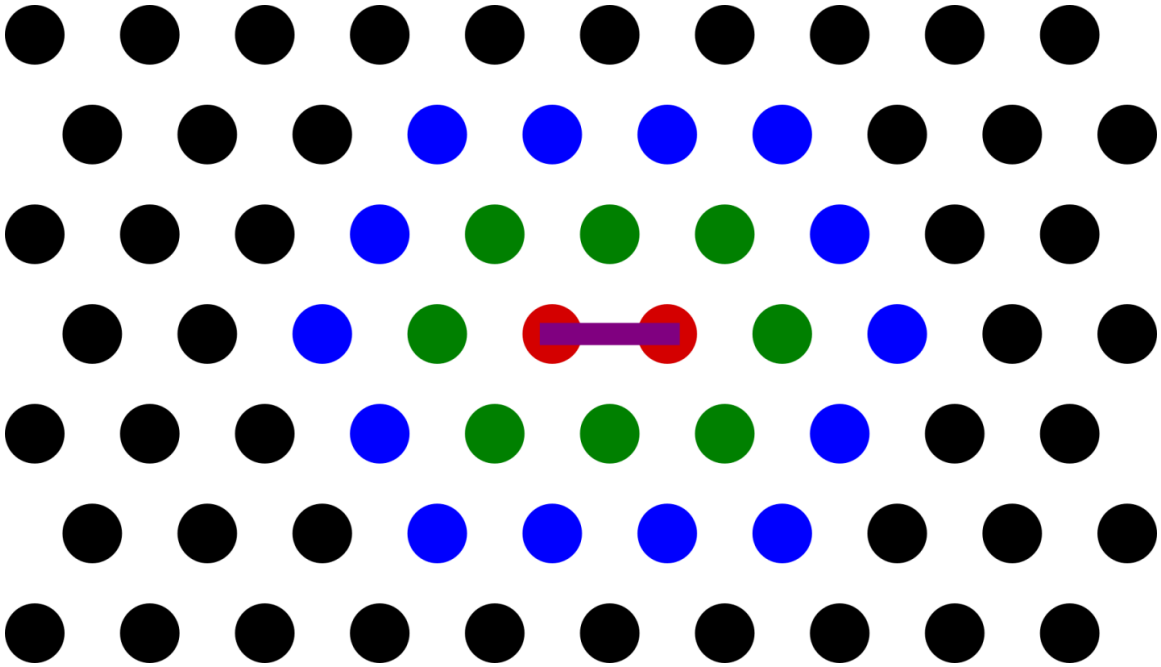

Figure A.6. Diagram for identifying whether a gold nanorod in the bridging state is at a defect in the hexagonal lattice or is not at a defect in the hexagonal lattice.

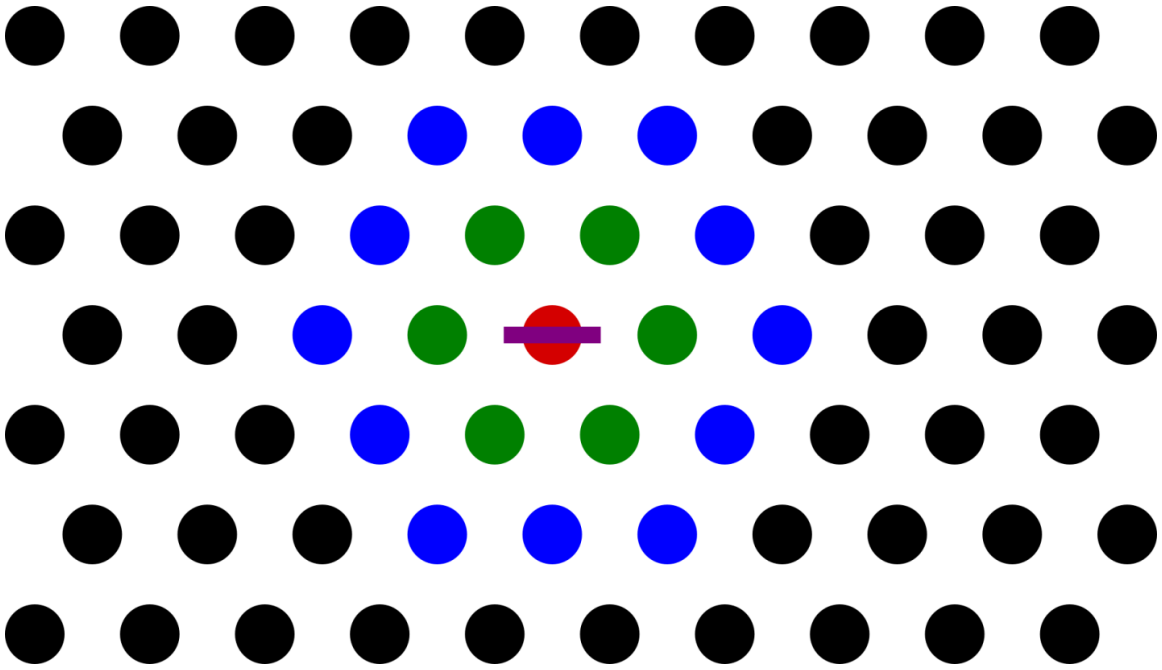

Figure A.7. Diagram for identifying whether a gold nanorod in the centered state is at a defect in the hexagonal lattice or is not at a defect in the hexagonal lattice.

MODEL DETAILS

Thin cylindrical AB-diblock copolymer nanocomposite films were modeled with a modified version of the Hybrid Particle-Field Theory method developed by Sides and coworkers.[1] The primary modifications are that nanorods are modeled with an anisotropic function[2], surfaces are included as cavity functions to simulate the confinement seen in a thin film[3,4], and polymer segment mass is distributed by a Gaussian smearing function[2–4] with standard deviation of 0.2 R_g, where R_g is the ideal radius of gyration of the diblock copolymer. The diblock copolymer chains are represented as discrete Gaussian chains with $N = N_A + N_B$ segments, where the statistical segment sizes and monomer volumes of the two blocks are assumed to be identical.

The discrete Gaussian polymer chain connectivity is modeled using the harmonic bonding potential

$$\beta U_0 = \sum_{i}^{n_D} \sum_{j}^{N-1} \frac{3\left|\mathbf{r}_{i,j} - \mathbf{r}_{i,j+1}\right|^2}{2b^2} \tag{1}$$

where n_D is the number of diblock chains and b is the statistical size of a polymer segment. Density deviations away from the bulk density, ρ_0, are penalized using a Helfand compressibility potential, given by

$$\beta U_1 = \frac{\kappa}{2\rho_0} \int d\mathbf{r} \left[\hat{\rho}_+(\mathbf{r}) - \rho_0\right]^2 \tag{2}$$

where $\hat{\rho}_+ = \hat{\rho}_{DA} + \hat{\rho}_{DB} + \hat{\rho}_{NR} + \hat{\rho}_W$ is the spatially varying total density and κ controls the strength of the density fluctuations. In the limit $\kappa \to \infty$, the strictly incompressible model is recovered. $\hat{\rho}_{DA}$, $\hat{\rho}_{DB}$, $\hat{\rho}_{NR}$, and $\hat{\rho}_W$ are the microscopic densities of the A-block of the diblock chain, B-block of the diblock chain, nanorods, and confining surface, respectively. The nanorods are treated as having A-like chemistry and are described by the anisotropic function

$$\hat{\rho}_{NR}(\mathbf{r}) = \frac{\rho_0}{4} \mathrm{erfc}\left[\frac{|\mathbf{u}\cdot(\mathbf{r}-\mathbf{r}_c)| - L_{NR}/2}{\xi_{NR}}\right] \mathrm{erfc}\left[\frac{|\mathbf{u}\times(\mathbf{r}-\mathbf{r}_c)| - R_{NR}}{\xi_{NR}}\right] \tag{3}$$

where $\mathbf{u}$ is the unit vector pointing in the long direction of the nanorod, $\mathbf{r}_c$ is the position of the nanorod center, L_{NR} is the nanorod length, R_{NR} is the nanorod radius, and ξ_{NR} is the length scale defining the distance over which the nanorod density drops from ρ_0 to 0. The confining surface is a soft wall of thickness T_W on the bottom and top of the simulation box, and is neutral to both A and B chemistries. It is described by the function

$$\hat{\rho}_W(\mathbf{r}) = \frac{\rho_0}{2} \mathrm{erfc}\left[\frac{\min(r_z, L_z - r_z) - T_W}{\xi_W}\right] \tag{4}$$

where r_z is the z-component of $\mathbf{r}$, L_z is the box size in the z-dimension, and ξ_W is the length scale over which the surface drops from a density of ρ_0 to a density of 0. A and B components are assumed to interact through a purely repulsive, Flory-like contact potential given by

$$\beta U_2 = \frac{\chi}{\rho_0} \int d\mathbf{r} \, [\hat{\rho}_{DA}(\mathbf{r}) + \hat{\rho}_{NR}(\mathbf{r})] \, \hat{\rho}_{DB}(\mathbf{r}) \tag{5}$$

where the Flory parameter χ quantifies the magnitude of incompatibility between A and B components.

We assume that the mass of each polymer segment maintains a Gaussian distribution about its center, such that $\hat{\rho}_K(\mathbf{r})$, the microscopic density of polymer segment type K, is given by

$$\hat{\rho}_K(\mathbf{r}) = \int d\mathbf{r}' h(\mathbf{r} - \mathbf{r}') \hat{\rho}_{K,c}(\mathbf{r}') = (h * \hat{\rho}_{K,c})(\mathbf{r}) \tag{6}$$

where $\hat{\rho}_{K,c}(\mathbf{r})$ is the distribution of polymer segment centers given by

$$\hat{\rho}_{K,c}(\mathbf{r}) = \sum_i^{n_K} \sum_j^{N_K} \delta(\mathbf{r} - \mathbf{r}_{i,j}), \tag{7}$$

$h(\mathbf{r})$ is the Gaussian smearing function given by

$$h(\mathbf{r}) = \left(\frac{1}{2\pi a^2} \right)^{3/2} e^{-|\mathbf{r}|^2/2a^2} \tag{8}$$

where a is the smearing length scale (0.2 R_g in this work), and the last expression in Equation 6 introduces our shorthand notation for a convolution integral.

By employing a standard Hubbard-Stratonovich particle-to-field transformation, we arrive at a partition function

$$\mathscr{Z} = z_1 \int \mathscr{D}\{w\} e^{\mathscr{H}[\{w\}]} \tag{9}$$

where z_1 is a numerical prefactor containing the thermal de Broglie wavelengths and normalization constants from the Gaussian functional integrals used to decouple the particle interactions, and $\mathscr{H}$ is the effective Hamiltonian given by

$$\begin{aligned} \mathscr{H}[\{w\}] = \frac{\rho_0}{2\kappa} \int d\mathbf{r} \; w_+(\mathbf{r})^2 - i\rho_0 \int d\mathbf{r} w_+(\mathbf{r}) - \int d\mathbf{r} w_A(\mathbf{r}) \hat{\rho}_{NR} \\ + \frac{\rho_0}{\chi} \int d\mathbf{r} \left[w_{AB}^{(+)}(\mathbf{r})^2 + w_{AB}^{(-)}(\mathbf{r})^2 \right] - n_D \ln Q_D \left[\mu_A, \mu_B \right] \end{aligned} \tag{10}$$

Here, $\{w\}$ represents the set of chemical potential fields $w_{AB}^{(+)}(\mathbf{r})$, $w_{AB}^{(-)}(\mathbf{r})$, and $w_+(\mathbf{r})$; μ_A and μ_B are defined by $\mu_K = (h * w_K)(\mathbf{r})$ where

$$w_A = i \left(w_+ + w_{AB}^{(+)} \right) - w_{AB}^{(-)}, \tag{11}$$

$$w_B = i \left(w_+ + w_{AB}^{(+)} \right) + w_{AB}^{(-)}, \tag{12}$$

Q_D is the partition functions for a single diblock chain. Q_D is calculated iteratively from the chain propagator $q(j,\mathbf{r})$,

$$Q_D[\mu_A,\mu_B] = \frac{1}{V}\int d\mathbf{r}\; q(P,\mathbf{r}) \tag{13}$$

with the chain propagator constructed using a Chapman-Kolmogorov equation

$$q(j+1,\mathbf{r}) = e^{-\mu_K(\mathbf{r})}\int d\mathbf{r}\;\Phi(\mathbf{r}-\mathbf{r}')q(j,\mathbf{r}) \tag{14}$$

where K is either A or B depending on the type of segment $j+1$ and $\Phi(\mathbf{r}-\mathbf{r}')$ is the normalized bond transition probability.

The set of mean-field equations describing this system can be written as

$$\frac{\partial\mathscr{H}}{\partial w_K} = 0 \tag{15}$$

where w_K represents any field w_+, $w_{AB}^{(+)}$, or $w_{AB}^{(-)}$. To compute mean-field solutions, we evolve the fields according to

$$\left(\frac{\partial w_K(\mathbf{r})}{\partial t}\right) = -\lambda_K\left(\frac{\partial\mathscr{H}}{\partial w_K(\mathbf{r})}\right) \tag{16}$$

where λ_K is the relaxation coefficient for field w_K and t is a fictitious time. We use a first-order semi-implicit scheme[5] to numerically evolve the fields. For each free energy calculation, the vertical distance between the nanorod and the surface played a significant role in the resulting free energy since the interfaces are "soft", in that the surfaces of each are essentially a smoothed step function. In order to prevent this effect from dominating the free energy, the vertical position of the rod relative to the surface was chosen to minimize the free energy using Brent's method in each simulation. Figure S8 shows the free energy calculations for all 3 nanorod sizes tested.

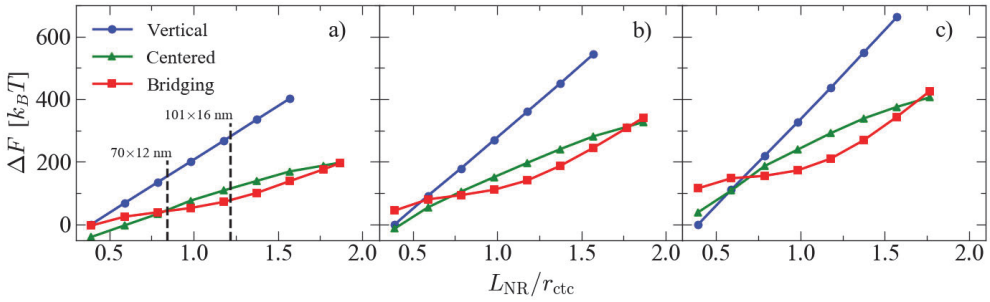

Figure A.8. Mean-field free energy differences for nanorods in different configurations as a function of nanorod length for nanorods of diameter a) 1.0 R_g, b) 1.5 R_g, and c) 2.0 R_g. The nanorod length in the x-axis is normalized by the cylindrical domain nearest neighbor center-to-center distance, r_{ctc}. Free energy differences in each plot are calculated relative to the free energy of a rod of the same diameter in the vertical configuration with a length of 2 R_g, the shortest length in each case. The positions of the 101x16 nm and 70x12 nm rods used in experiments are marked in a) to show roughly where the experimental nanorod sizes fit into these calculations.

REFERENCES

[1]S. W. Sides, B. J. Kim, E. J. Kramer, and G. H. Fredrickson, Physical Review Letters **96**, 250601 (2006).

[2]J. Koski, H. Chao, and R. A. Riggleman, Journal of Chemical Physics **139**, 244911 (2013).

[3]H. Chao, B. A. Hagberg, and R. A. Riggleman, Soft Matter **10**, 8083 (2014).

[4]J. Koski, H. Chao, and R. A. Riggleman, Chem. Commun. **51**, 5440 (2015).

[5]E. M. Lennon, G. O. Mohler, H. D. Ceniceros, C. J. García-Cervera, and G. H. Fredrickson, Multiscale Modeling and Simulation **6**, 1347 (2008).